Morphological Evolution of Debris Disks

「デブリ円盤の形態進化」

2015 年度

蔡 承 亨

兵庫県立大学大学院物質理学研究科

Abstract

Debris disks are circumstellar disks that mainly contain dusts. The dust grains are thought to be produced by the collisions of excited planetesimals. Approximately 15% of the main sequence stars have debris disks, of which 26 are spatially resolved at the optical and near-infrared (NIR) wavelengths. By investigating the morphological evolution of debris disks, we can better understand planetary formation.

Three mechanisms of planetesimal stirring have been proposed: 1) close stellar flybys, 2) planetary stirring, and 3) self-stirring. To verify these stirring theories, researchers have conducted many infrared photometric and far-infrared imaging observations. However, in these observations, the stirring theories were poorly constrained by the large uncertainty of the disk radius ($\gtrsim$ tens of AU). Thus, to properly evaluate the stirring theories, we investigate the disk morphologies by visible or NIR imaging observations.

We investigate 22 debris disk morphologies and detected the debris disk of HD 15115 using Subaru/IRCS. We also retrieve the raw archival data of seven targets and obtain a final processed image of HD 202628 from the author of a previous study.

We resolve the HD 15115 disk by subtracting the PSF halo and obtain its disk parameters (disk radius, vertical thickness, inner/outer density slopes, scattering asymmetry parameter, inclination, and disk position angle) by disk model fitting. Based on the study of HD 15115, we also probe other eight other debris disk geometries using archival data.

The disk radii, which were resolved to several AU, seem to increase with stellar age and stellar mass. The vertical thicknesses also increase with stellar age. Furthermore, the inner and outer density slopes trend upward with increasing stellar mass. The upper limits of the scattering asymmetry parameter seem to decrease with stellar age.

The increasing trends of disk radius relative to the stellar age and mass are consistent with the self-stirring scenario. We examine the possibilities of planetary stirring around three debris disks containing detected planets. The planetary stirring model can explain only the presence of the inner disk of beta Pic (at radius $\propto$ 60 AU) by a $\propto 10 M_J$ planet ($\propto$ 9 AU). The vertical thickness is approximately proportional to the disk radius, whereas the velocity dispersion might be independent of age and mass. The disk ring widths become thinner for more massive stars, suggesting that more massive stars have shorter collision durations. The deceasing upper limit of the asymmetry parameter can be due to disappearance of larger grains or observational bias.

Acknowledgement

I would like to thank all the people who supported me along the way. First, I am deeply grateful to my advisor Prof. Yoichi Itoh for giving me the chance to study astronomy and for enthusiastically guiding me. I would like to thank the vice-chairmen Prof. Hiroshi Shibai, Prof. Yoshinori Takahashi, Prof. Kenji Honma, and Dr. Toshihito Ishida, for their meaningful comments. Prof. Hiroshi Shibai also taught me the basic of this study in my master's course.

I would also like to thank all members of the Nishi-Harima Astronomical Observatory, University of Hyogo, for fruitful discussion and for supporting my research for three years. I would also like to express my gratitude to the IRAL members of Osaka University, especially Dr. Misato Fukagawa, who provided the opportunity to study debris disks.

The observations of HD 15115 were made with the Subaru Telescope, which is operated by the National Astronomical Observatory of Japan. I thank the telescope operators and the AO188 team for performing the observations. I also thank Dr. Thayne Currie, the PI of this observation, for providing me with data and for the meaningful discussions. I am also grateful to Dr. John Krist, Dr. Zahed Wahhaj, and Dr. Esther Buenzli for providing me with the final disk image data. I also thank the Astronomical Society of Japan for supporting my traveling expenses (the 86th Hayakawa Satio Fund) to the international workshop held in Paris. I would also like to thank Enago (www.enago.jp) for the English language review.

Finally, I would like to thank my friends in Sayo and my family for supporting me. I am deeply grateful again to all of the people who helped me accomplish my doctoral thesis.

Contents

1 Introduction

1.1 Planetary formation

This thesis focuses on *debris disks*, which are related to planetary formation. First, we briefly describe what is already known about planetary formation and the origin of debris disks.

A protostar is born when a molecular cloud in space begins collapsing under gravity. The matters in the cloud fall into the core (protostar) with random orbiting. The orbital angular momentum vector of the matters roughly points in a certain direction, forming a disk composed of gas and dust. Within this so-called *protoplanetary disk*, the dust accretes into planets and planetesimals. After $\propto$ 1 10 Myr, all of the gas in the protoplanetary disk has accreted onto the star or disappeared through stellar photoevaporation. The dust grains also have disappeared at this stage, leaving only planets and planetesimals in the system. Once the protoplanetary disk has disappeared, the formed planets and planetesimals collide because their movements are no longer limited by the gas. The dust grains ejected from the collisions form a disk. Such secondarily emergent disks are called *debris disks*.

1.2 Debris disks

As debris disks have temperatures of several tens of Kelvins, debris disks are luminous at mid- to far-infrared wavelengths. Debris disks were discovered by the Infrared Astronomical Satellite (IRAS) in the 1980s. In honor of the first discovered target, Vega (Figure 1; Aumann et al. 1984), stars with debris disks are called *Vega type stars*. Approximately 15% of the main sequence stars are Vega type stars (e.g., Matthews et al. 2014).

According to spectral energy distribution (SED) observations, the typical temperature of Vega type stars is $\propto$ 40 100 K; therefore, dusts locate at $\propto$ 10 100 AU (e.g., Zuckerman and Song 2004). The total dust mass in a disk is estimated as $\propto 10^{-3}$ $10^{-1} M_{\odot}$ (Rhee et al. 2007). Radio spectroscopic observations suggest that most debris disks are CO-poor ($< 10^{-4} M_{\odot}$; Moór et al. 2011a). However, two debris disks, HD 21997 and 49 Cet, contain significant CO gas ($\gtrsim 10^{-4} M_{\odot}$; Moór et al. 2011a, Zuckerman and Song 2012).

Debris disks scatter the starlight at visible and near-infrared (NIR) wavelengths, and thermally emit at mid-infrared to millimeter wavelengths. The disk morphology is difficult to image because debris disks are faint. About 80 debris disks have been spatially resolved so far (Choquet et al. 2015). The first observed star containing a resolved disk was beta Pic (Figure 2; Smith and Terrile 1984), which was imaged at 890 nm with a du Pont 2.5 m telescope. After this discovery, no further debris disks were resolved for a long time. Most of the debris disks have been imaged since the 2000s, typically ($\propto$70%) at mid-infrared to millimeter wavelengths. Only 26 disks have been resolved at visible or NIR wavelengths.

Although the diffraction limit of large-aperture telescopes at visible or NIR wavelengths is $\lesssim$ 0.1", stellar images are blurred by the atmospheric turbulence. To obtain images at the diffraction-limited resolution, we must observe objects using space telescopes or large ground-based telescopes with adaptive optics. The representative space telescope is the Hubble Space Telescope, and famous ground-based telescopes are Subaru, Gemini, and the Very Large Telescope. To detect faint disks, we must also enhance the contrast by observational and data reduction techniques. The predominantly bright stellar halo is usually suppressed by a coronagraph mask. To distinguish the faint disk

components from the halo and artifacts of the optical system, we apply a common observational method, called angular differential imaging (ADI; Marois et al. 2006; See section 2). Especially, we use classical ADI (cADI; Marois et al. 2006) to subtract the stellar halo and highlight the disk in the data reduction (see Section 3.1). Recently, principal component analysis (PCA; Soummer et al. 2012) has become a powerful tool for clearly subtracting the stellar halo (see Section 3.1 and Appendix A).

Direct imaging observations suggest a ring-like structure for most debris disks. In addition, many debris disks have structural characteristics such as warps, offsets, and asymmetric brightness, which are considered to be related to gravitational interaction between the disk and planets. In fact, planets have been detected in several debris disk systems, e.g., beta Pic b (Lagrange et al. 2009), HD 10647 b (Butler et al. 2006), and HD 106906 b (Bailey et al. 2014).

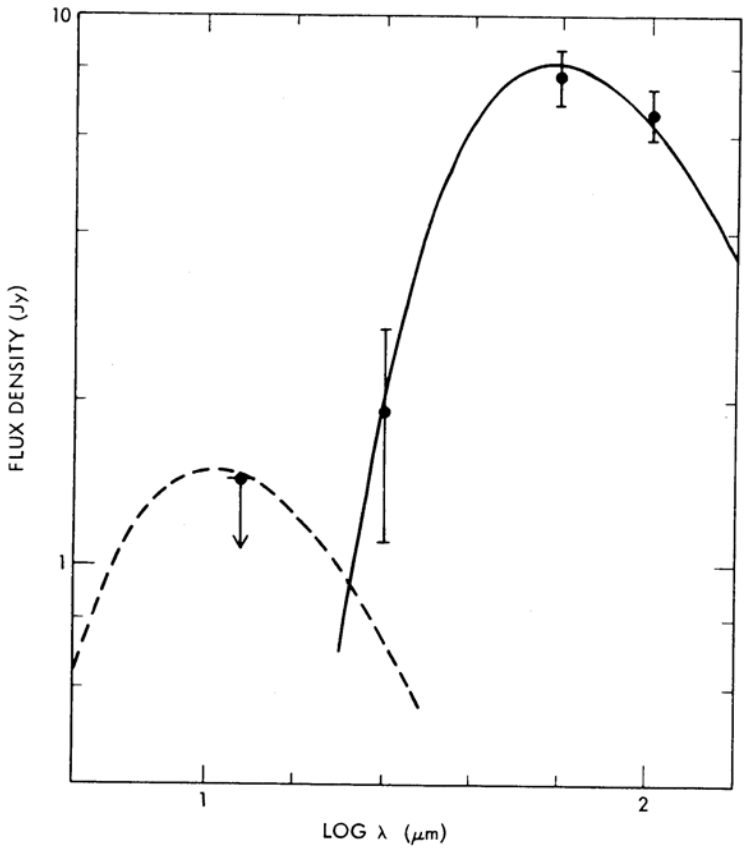

Figure 1: Spectral energy distribution of Vega. Solid and dashed lines represent an 85 K and a 500 K blackbody spectrum, respectively. The 85 K spectrum implies that the dust grains are located at ∝85 AU from Vega. Figure from Aumann et al. (1984).

1.3 Debris disks in our solar system

Dust grains in the solar system are evidenced from the populations of asteroids and Kuiper belt objects. The zodiacal dust can be regarded as a debris disk. According to observations with the

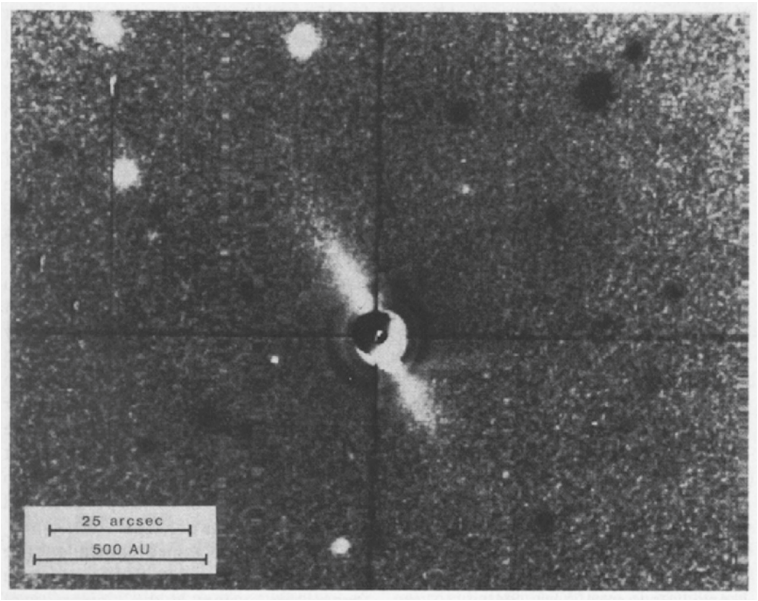

Figure 2: Resolved image of the beta Pic debris disk. North is at the top. The edge-on disk extends 400 AU to the northeast and southwest of the star, which is located behind a coronagraph mask. Figure from Smith and Terrile (1984).

IRAS, COBE, ISO and Spitzer space telescopes, the dust fractional luminosity $L_{\rm dust}/L_{\circ}$ is $\propto 4 * 10^{-8}$ (Dermott et al. 2002, Moro-Martin 2013). The zodiacal dust grains are believed to originate from asteroid collisions and comets, but might also be sourced from Kuiper belt objects. However, the thermal emission of grains from the Kuiper belt is undetectable, being overwhelmed by the much brighter zodiacal light in the foreground. Dynamical modeling of dust production in the Kuiper belt, combined with recent in situ detections by the New Horizons spacecraft, estimates the dust fractional luminosity of the Kuiper belt as $L_{\rm dust}/L_{\circ} = 1.2 * 10^{-7}$ (Vitense et al. 2012, Moro-Martin 2013).

The dust grains harbored in our solar system might have been as numerous as those observed in extra-solar debris disks. Therefore, observations of debris disks might provide the collisional history of planetesimals in our solar system.

1.4 Stirring mechanisms

The lifetime of dust particles is much shorter than the stellar age. For example, the Poynting-Robertson drag pulls a micron-sized dust grains at 40 AU into a solar-type star in $\propto$3 Myr (Moro-Martin 2013). Therefore, planeteimals frequently collide in debris disk systems. Such frequent collisions are induced by dynamical stirring, but the origin of stirring remains unclear. Elucidating the stirring mechanism is important for understanding planetary formation in our own solar system. Thus, many researches have approached this theme from theoretical and observational perspectives.

1.4.1 Theoretical predictions

Stirring can occur by one of the following three mechanisms:

1. Close stellar flybys
2. Planetary stirring
3. Self-stirring

In the first stirring model, dynamical excitation is triggered by a close stellar encounter. Assuming that planetesimals had been excited by a flyby star at 30-150 AU, Kenyon and Bromley (2002) simulated the time evolution of the dust luminosity. They set the initial eccentricity and inclination of the planetesimals as $e_0 = 0.01 \quad 0.06$ and $i_0 = e_0/2$, respectively. They expressed the dust luminosity in terms of two constants c_1 and c_2:

$$\frac{L_{\rm dust}}{L_{\pm}} = \frac{L_0}{c_1 + (t/t_d)^{c_2}} \ . \tag{1}$$

The maximum dust luminosity L_0 and the damping time $t_{\rm d}$ depend on the disk mass: $L_0 \ \infty \ M_{\rm d}$, $t_{\rm d} \ \infty \ M_{\rm d}{}^{1}$. At a planetesimal disk mass of 0.01-1 times the minimum mass solar nebular, Kenyon and Bromley's calculations yield $t_{\rm d} \propto$1-10 Myr (with $c_1 \propto$1-2, $c_2 = 1$, and $L_0 \propto 10^{\ 3}$-$10^{\ 5}$). They concluded that the stellar flyby scenario is consistent with the luminosities of observed debris disk aged $\propto$ 10 Myr. However, they also considered that such events are too rare to explain collisional cascades in $\gtrsim$ 100 Myr debris disks .

In the second stirring model, dynamical excitation is triggered by a massive planet in the system. Using secular perturbation, Mustill and Wyatt (2009) calculated the time at which two planetesimals begin to cross each other. The crossing timescale was derived as

$$\begin{aligned} t_{\rm cross} \ &\propto \ 1.53 * 10^3 \frac{(1 \quad e_{\rm p}^2)^{3/2}}{e_{\rm p}} \left(\frac{r}{10 \text{ AU}}\right)^{9/2} \left(\frac{M_{\pm}}{M_{\circ}}\right)^{1/2} \left(\frac{M_{\rm p}}{M_{\circ}}\right)^{\ 1} \left(\frac{a_{\rm p}}{1 \text{ AU}}\right)^{\ 3} \text{yr} \\ &= \ 405 \ \frac{(1 \quad e_{\rm p}^2)^{3/2}}{e_{\rm p}} \left(\frac{r}{100 \text{ AU}}\right)^{9/2} \left(\frac{M_{\pm}}{M_{\circ}}\right)^{1/2} \left(\frac{M_{\rm p}}{M_J}\right)^{\ 1} \left(\frac{a_{\rm p}}{5 \text{ AU}}\right)^{\ 3} \text{Myr}, \end{aligned} \tag{2}$$

where $e_{\rm p}$, $M_{\rm p}$, and $a_{\rm p}$ are the eccentricity, mass, and semi-major axis of the planet, respectively. Equation (2) indicates that the planetesimals cross from the inside to the outside, and that the propagation speed of the planetesimals' crossing decrease with increasing stellar mass. Moreover, $t_{\rm cross}$ largely depends on the planetary masses and orbital elements.

In the third stirring model, dynamical excitation is triggered by naturally formed 1000 km bodies in the system. Kenyon and Bromley (2008) derived the formation timescale of a 1000 km body as

$$t_{1000} \propto 145 x_m{}^{1.15} \left(\frac{r}{80 \text{ AU}}\right)^3 \left(\frac{M_{\pm}}{2M_{\circ}}\right)^{\ 3/2} \text{Myr}, \tag{3}$$

where x_m is the scaling factor relative to the surface density of the minimum-mass solar nebula. Thus, the initial surface density distribution can be written as

$$\Sigma(r) = 0.18 \left(\frac{M_{\pm}}{M_{\circ}}\right) x_m \left(\frac{r}{30 \text{ AU}}\right)^{\ 3/2} \text{g/cm}^2. \tag{4}$$

Equation (3) suggests that gravitational scattering begins close to the star and moves outward to large distances from the star. The scattering propagates more rapidly for more massive stars.

1.4.2 Observational approaches

The above stirring theories have been evaluated in many observational studies. Najita and Williams (2005) examined the correlation between the stellar age and the disk radius derived from SED. The obtained disk radii of 18 stars (from early- to late-type) were uncorrelated with stellar age. Conversely, Rhee et al. (2007) derived the SED disk radii of $\propto$35 early-type stars (B and A), and found that disk radius increases with age. Moór et al. (2011b) and Eiroa et al. (2013) reported the same trend in 26 F-type stars and 30 FGK type stars (Herschel far-infrared images). Chen et al. (2014) derived the disk radii of $\propto$600 B9-K5-type stars (corresponding to 0.5-5.5 $M_\odot$) by SED fitting. They concluded that old and young stars are inconsistent with the self-stirring hypothesis. Moór et al. (2015) obtained Herschel-resolved disk images of 11 stars ranging between B9 and F7. They considered that seven of their disks fitted the self-stirring scenario; the remaining four targets were potential candidates for planetary stirring.

The conflicting conclusions of previous studies can be attributed to the large uncertainty in the disk radius ($\gtrsim$ several tens of AU). The uncertainties in SED disk radii are increased by the many degenerate parameters (e.g., dust size, grain composition, and volume density profile). The spatial resolution of far-infrared imaging observations is limited by the large diffraction limit. Therefore, more accurate disk radii are necessary to constrain the stirring mechanisms.

1.5 Ring width

How a planet decides the debris disk morphology has been investigated in several studies. The ring width is one determiner of planet mass. Chiang et al. (2009) reproduced the observed disk structure of Fomalhaut, which contains a planet. They showed that the disk ring width increases with planet mass, and constrained the planet mass to $M_\mathrm{p} < 3\ M_J$ in the Fomalhaut system. A faint object has also been detected in this system (Kalas et al. 2008, Currie et al. 2012a, Galicher et al. 2013). However, Kalas et al. (2013) reported that the orbit of Fomalhaut b is sufficiently eccentric, with $e_p = 0.8 \oplus 0.1$ and $a_p = 177 \oplus 68$ AU, to penetrate the disk. Thus, Fomalhaut b is unlikely to shape the disk structure.

Rodigas et al. (2014) derived the relation between the ring width and planet mass in dynamical N-body simulations:

$$M_\mathrm{p}/M_J \geq \left(\frac{\Delta R_\mathrm{d}/R_\mathrm{d} \quad (0.107 \oplus 0.032)}{0.019 \oplus 0.0064}\right)\left(\frac{M_\pm}{M_\odot}\right), \tag{5}$$

where ΔR_d and R_d denote the ring width and radius of the debris disk, respectively. They predicted the upper limits of the planet masses in five systems (Fomalhaut, HR 4796A, HD 207129, HD 202628, HD 18327). However, no planets have been detected in these five systems (e.g., Wahhaj et al. 2013, Rodigas et al. 2015), possibly because of poor detection sensitivity. Meanwhile, the ring width might depend on factors other than planet mass.

1.6 Aims

This thesis presents high-resolution imaging observations of debris disks at visible and NIR wavelengths. Using a common disk model, we resolve the disk radius to less than several AU. We also derive the ring widths of the debris disks. We aim to investigate the relations between disk parameters and stellar age or mass. Chapter 2 is devoted to the selection and observations of our targets;

we especially observed the debris disk around HD 15115. The data reduction and disk model fitting, which comprise the greater part of this study, are described in Chapter 3. In Chapter 4, we present the results of the disk parameters and compare the derived disk radii with those of SED observations. Chapter 5 discusses the calculated ring widths and the stirring models supported by our results. The thesis concludes with a results summary and discussion in Chapter 6.

2 Targets and Observations

2.1 Targets

We investigated the geometries of 22 ring-like debris disks. We selected main-sequence stars and possible main-sequence stars (age $\gtrsim$ 10 Myr) with disks that were spatially resolved at visible or NIR wavelengths. The observations and derived disc image of HD 15115 are presented in Sections 2.3 and 3.2, respectively. The processed disk image data of HD 202628 were obtained from John E. Krist. We also retrieved the raw archive data of Fomalhaut, HR4796A, HD207129, HD 141943, HD 10647, HD 61005 and HD 139664, and processed them into disk images. The disk parameters of the other targets were borrowed from previous studies of direct imaging.

The stellar properties of the targets are summarized in Table 1. In this table, the age ranges from $\propto$ 10 Myr to $\propto$ 3 Gyr and the mass ranges from 0.4 $M_{\circ}$ to 2.5 $M_{\circ}$.

2.2 Observations

All of the targets acquired using a ground-based telescope were observed in the ADI mode (Marois et al. 2006). The ADI mode continuously aligns the instrument with the telescope optics, while the field of view is allowed to rotate by diurnal motion. The HST data are acquired in the same way. The different roll angles of the orbiting spacecraft with fixed instrumental artifacts provide different orientations of the sky. As the only rotating perspective is the field of view, faint disks can be distinguished from the predominantly bright halo of the star and the artifacts from the optical system.

Table 2 lists the targets whose disk morphologies were derived in this study. The central wavelength λ_c is 0.6 μm or 1.6 μm, $t_{\rm exp}$ is the total exposure time, and $\theta_{\rm rot}$ is the rotation angle of the field of view. HD 139664 and Fomalhaut, which were observed in multiple days, occupied $123^{\leq}$ and $162^{\leq}$ of the field rotation over all observations, respectively.

2.3 Observation of HD 15115

H-band (1.63 μm) images of HD 15115 were acquired by the Infrared Camera and Spectrograph (IRCS) onboard the Subaru telescope (Nasmyth focus stage; AO 188 adaptive optics system) on UT November 11, 2011. The detector was the ALADDIN Ⅲ 1024 $*$ 1024 InSb array. The pixel scale was 20.57 mas/pixel, corresponding to a field of view of 21.06" $*$ 21.06". The sky was covered with cirrus throughout the observations. The H-band magnitude of the star was 5.86. The full width at half-maximum (FWHM) of the stellar point spread function (PSF) was $\propto$0.1", with a suspected variation of $\lesssim$0.05". This spatial resolution is within the permissible range of disk detection, although it is not diffraction-limited. The flux of the central star was reduced by a 0.8" diameter coronagraph mask. Observations were made in the ADI mode. Each of the obtained 82 frames was coadded with 2.0 s exposure images in four non-destructive readouts (NDRs). The numbers of COADDs in the first 10 frames and the remaining 72 frames were 20 and 10, respectively. The total integration time was 30.7 min, and the rotation angle of the field of view was $\propto 17.3^{\leq}$.

Table 1: Stellar properties of targets

Target	t (Myr)	t_{min} (Myr)	t_{max} (Myr)	$M_{\pm}$ ($M_{\circ}$)	Sp.type	Age reference	Mass reference
TWA 7	10	4.4	13	0.37	M3.2	(1)	(2)
AU Mic	21	15	28	0.45	M1	(3)	(4)
TWA 25	10	7	13	0.63	M0.5	(1)	(5)
HD 35650	100	50	200	0.63	K6V	(1)	(4)
HD 92945	150	80	300	0.81	K1V	(6)	(7)
HD 61005	90	50	130	0.93	G8V	(8)	(7)
HD 107146	140	80	200	1.04	G2V	(6)	(9)
HD 202628	2300	1300	3300	1.04	G2V	(10)	(9)
HD 377	200	147	250	1.05	G2V	(1)	(9)
HD 207129	2300	1500	3200	1.08	G0V	(11)	(11)
HD 10647	2900	1300	3700	1.10	F8V	(12)	(9)
HD 141943	25	17	32	1.20	G2V	(13)	(14)
HD 15115	100	12	500	1.32	F2	(15)	(16)
HD 181327	21	15	28	1.33	F6V	(3)	(7)
HD 139664	300	100	1000	1.36	F5V	(6)	(16)
HD 115600	15	15	15	1.40	F2V/F3V	(17)	(17)
HD 106906	13	11	15	1.50	F5V	(18)	(18)
beta Pic	21	15	28	1.75	A5	(3)	(19)
HD 32297	30	30	30	1.84	A5	(20)	(20)
HD 131835	15	15	15	1.90	A2IV	(21)	(21)
Fomalhaut	440	400	480	1.92	A4/A3	(22)	(22)
HR 4796A	9	8	10	2.53	A0	(23)	(24)

References

(1) Choquet et al. 2015; (2) Manara et al. 2013; (3) Binks and Jeffries 2014; (4) Shaya and Olling 2011; (5) Gaidos et al. 2014; (6) Schneider et al. 2014; (7) Casagrande et al. 2011; (8) Buenzli et al. 2010; (9) Takeda et al. 2007; (10) Krist et al. 2012; (11) Marshall et al. 2011; (12) Valenti and Fischer 2005; (13) Soummer et al. 2014; (14) Chen et al. 2014; (15) Rodigas et al. 2012; (16) Allende Prieto and Lambert 1999; (17) Currie et al. 2015; (18) Kalas et al. 2015; (19) Lagrange et al. 2010; (20) Donaldson et al. 2013; (21) Hung et al. 2015; (22) Kalas et al. 2013; (23) Wahhaj et al. 2014; (24) De Rosa et al. 2014

Table 2: Observations

Target	Instrument	λ_c (μm)	Date	$t_{\rm exp}$ (s)	$\theta_{\rm rot}$ (degree)	Reduction
HD 61005	VLT/NACO	1.6 (H)	2010/2/17	2517.0	112	PCA
HD 202628	HST/STIS	0.6 (no filter)	2011/5/15	4512.0	28	roll-subtraction
HD 207129	HST/ACS	0.6 (F606W)	2006/5/3	4160.0	20	roll-subtraction
HD 10647	HST/ACS	0.6 (F606W)	2006/9/2	4660.0	25	roll-subtraction
HD 141943	HST/STIS	0.6 (no filter)	2014/7/23	3399.6	15	roll-subtraction
HD 15115	Subaru/IRCS	1.6 (H)	2011/11/11	1840.0	17.3	PCA
HD 139664	HST/STIS	0.6 (no filter)	2011/5/23	5621.4	48	PCA
		0.6 (no filter)	2011/7/31	5621.4	42	PCA
Fomalhaut	HST/STIS	0.6 (no filter)	2010/6/13	1260.0	25.9	cADI
		0.6 (no filter)	2010/9/13	3000.0	24	cADI
		0.6 (no filter)	2012/5/29-31	10080.0	28	cADI
		0.6 (no filter)	2013/05/30	9072.0	28	cADI
HR 4796A	Gemini/NICI	1.6 (H)	2012/4/6	4386.7	82.4	PCA

3 Analyses

3.1 Data reduction

The unprocessed images were subjected to dark subtraction, flat-fielding, bad-pixel correction, and cosmic-ray rejection. The images used for HST data had been already processed by these basic calibrations. To minimize the residual sum-of-squares of the pixel values in the PSF, we aligned the star position in each science frame.

After the star alignment, the disk was highlighted by subtracting the halo from the science frames. The PSF reference images (halo templates) were constructed by three methods:

1. cADI (Marois et al. 2006)
2. PCA (Soummer et al. 2012)
3. Roll subtraction (Krist et al. 2010, 2012)

PCA or cADI was applied to fields of view with more than two position angles (PAs), whereas roll subtraction was applied to fields of view with only two orientations. Locally optimized combination of images (LOCI; Lafrenière et al. 2007) was not performed because the optimized subsection might limit the disk shape in the final image.

cADI, which median-combines the complete set of science frames, is the simplest method for building PSF reference images. Frame screening of the individual science images was not applied. To adjust the variance of the PSF FWHM, we scaled the median-combined image at every annulus with a one-pixel width to suit each science frame.

Initially, we performed cADI reduction of all targets with more than two PAs. However, cADI usually generates PSF residuals. In such cases, the images were re-processed by PCA, which clearly subtracts the PSF while retaining the disk signals (see Appendix A for more details). Based on a specified field rotation criterion, we selected the science frames for building a PSF reference image. Next, we derived the eigenvector images (principal components) from the selected science frames by singular value decomposition. Finally, we linearly combined these eigenvector images into the PSF reference image. This process was performed for each science frame.

When the field of view has two orientations, the roll subtraction method can extract almost complete disk signals. Our roll subtraction procedure is similar to that of Krist et al. (2010, 2012). We build an initial template by comparing the corresponding pixel values in two different orientation frames and selecting the smaller value. We then subtract this template from each science frame. Next, we rotate one of the residual images to fit the orientation of the other. The smaller pixel values between these two residual images are recorded onto a disk template, which is subtracted from each science frame. This routine is iterated until the PSF template changes by less than a specified amount.

After building the PSF reference images by methods 1, 2, or 3, we subtracted each PSF reference image from each science frame. Finally, we aligned the PA by rotating the PSF-subtracted science frames and median-combined them into a high-signal-to-noise disk image. For the targets observed across multiple days (HD 139664, Fomalhaut), we combined all dataset images into a single final image. The processed disk images are presented in Figure 3.

3.2 Data reduction of HD 15115

The PSF reference images were extracted by PCA. For this purpose, we used the pipeline[1] published by Dmitri Mawet. First, we masked the inner region (r ≦ 40 pixels = 0.82”), and then divided each science image into concentric ring subsections of one-pixel width. The eigenvectors were calculated in each ring subsection. This calculation is tuned by two parameters, the number of PCA modes n and the distance N_δ (in units of PSF FWHM). Frames separated by more than N_δ were built into the PSF reference image. The construction of n PCA modes requires at least n frames. In contrast, the number of available frames decreases with increasing N_δ. Therefore, when n is set, N_δ imposes an upper limit on the PSF reference image construction of the n frames. For example, when $n = 5$, the constraint $N_\delta \leqq 1.054$ ($\propto$0.1”) allows no more than five reference frames for all science images at $r > 40$ pixels. In PCA processing, we tried $n = 1$ to $n = 40$. To protect the disk signal from self-subtraction, we set value of N_δ to the maximum. The disk S/N was maximized at $\propto$ 1.5” for $n = 15$ and $N_\delta = 0.751$. In this study, the HD 15115 disk was analyzed using the final image derived with these two parameters.

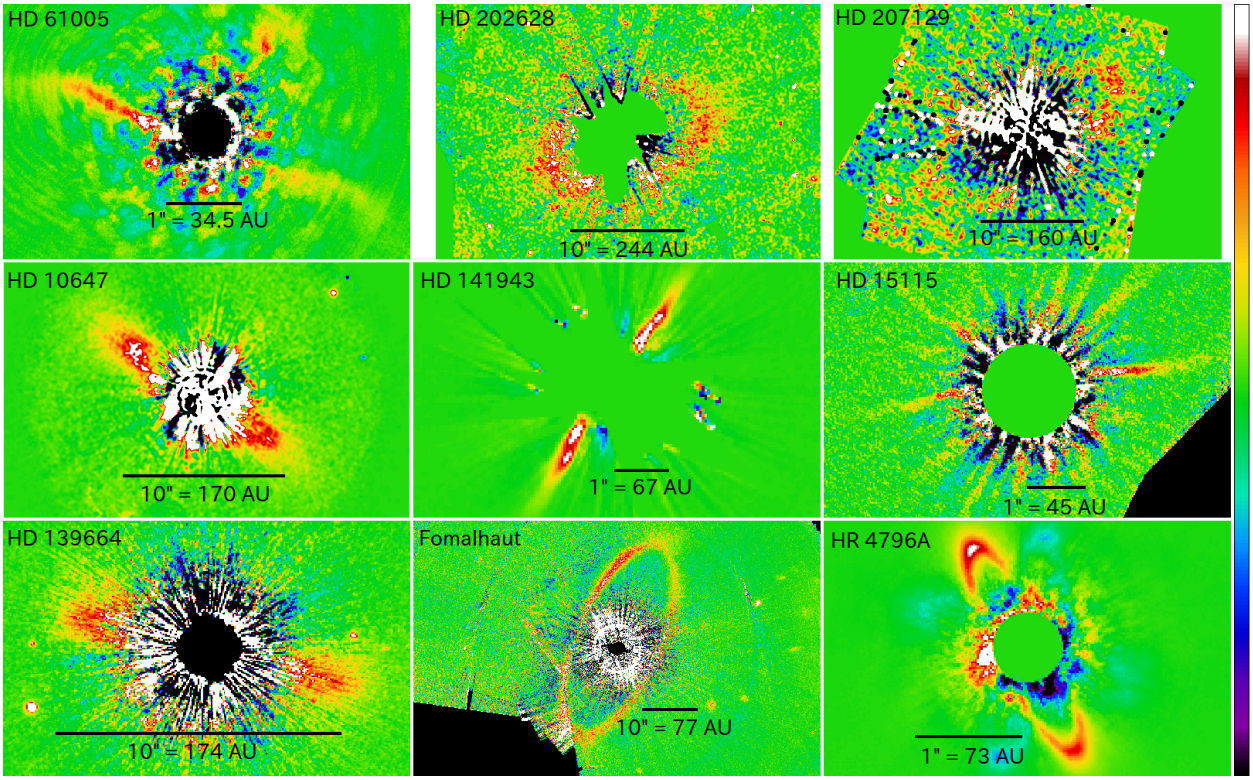

Figure 3: Resolved disk images. In all images, north is up, and east is left. The intensity scales are adjusted for individual disk brightness.

[1] http://www.sc.eso.org/~dmawet/pca-pipeline.html

3.3 Self-subtraction

When the rotation angle of the field of view is small, the disk can be accidentally subtracted along with the PSF reference image (e.g., Milli et al. 2012). In this study, self-subtraction calibration was not required because the rotation angles of the field of view were sufficiently large for most targets. However, edge-on disks located at small projected distances from the star were self-subtracted to some extent. As HD 141943 and HD 15115 were viewed edge-on disks with a small field roatation angle ($\theta_{\rm rot} < 20^{\leqq}$), the disk in the final images of both targets are likely to be self-subtracted.

3.3.1 Self-subtraction in HD 141943

The HST image set of HD 141943 has two different orientation frames of the field of view. Therefore, both frames were processed by roll subtraction. To simulate self-subtraction of the HD 141943 disk, we added an artificial disk (a rectangular object) to each science frame and recovered the disk by roll subtraction. The artificial disk was placed at the location of the detected disk, but was $\propto$100 times brighter than the detected disk. The pixel width w was set to 5 or 10 pixels. The results of the self-subtraction simulation are presented in Figure 4. For w = 5, the artificial disk outside the projected distance of a = 19 pixels fully recovered the original intensity, whereas the region within the projected distance suffered from self-subtraction. Doubling w to 10 pixels yielded the same behavior with a boundary a = 38 pixels. This result is perfectly consistent with the following simple assumption. For a disk of projected width w at a projected distance a, self-subtraction occurs wherever

$$w(a) > a\theta_{\rm rot}. \tag{6}$$

Therefore, for HD 141943 ($\theta_{\rm rot} = 15^{\leqq}$), disk loss occurs at $a < w/\theta_{\rm rot}$ = 19 pixels (w = 5 pixels) and 38 pixels (w = 10 pixels).

However, the width of the observed disk is $\propto$ 5 pixels, with a > 40 pixels = 2.0" (corresponding to 35 AU). Assuming that w = 5 pixels at every a, self-subtraction should thicken or thin the inner side (a < 19 pixels = 0.86" (16 AU)) of this disk. Therefore, the vertical thickness of the HD 141943 disk might be unreliable. Meanwhile, the disk radius of HD 141943 should be correct because the HD 141943 disk is imperfectly edge-on. Therefore, the disk radius was determined by the curve of the disk in the mid-plane (disk position) rather than the disk width.

3.3.2 Self-subtraction in HD 15115

In our published paper (paper 1), we simulated self-subtraction in artificial disks. We prepared nine types of rectangular disks with three intensities (0.5, 1.0, and 2.0 ADU = 0.11, 0.22, and 0.44 mJy/arcsec^2) and three widths (w = 5, 10, and 15 pixels). After adding the rectangular disk to each science frame, we recovered and processed the disk, and then measured their intensities and widths at each projected distance. In the self-subtraction simulations, both the intensity and width mainly depended on the original width of the disk. Finally, we derived the scaling factors, the uncertainties in the disk surface brightness, and the FWHM. We calibrated the disk surface brightness and FWHM, and then obtained the disk geometry parameters (see Section 3.4.3).

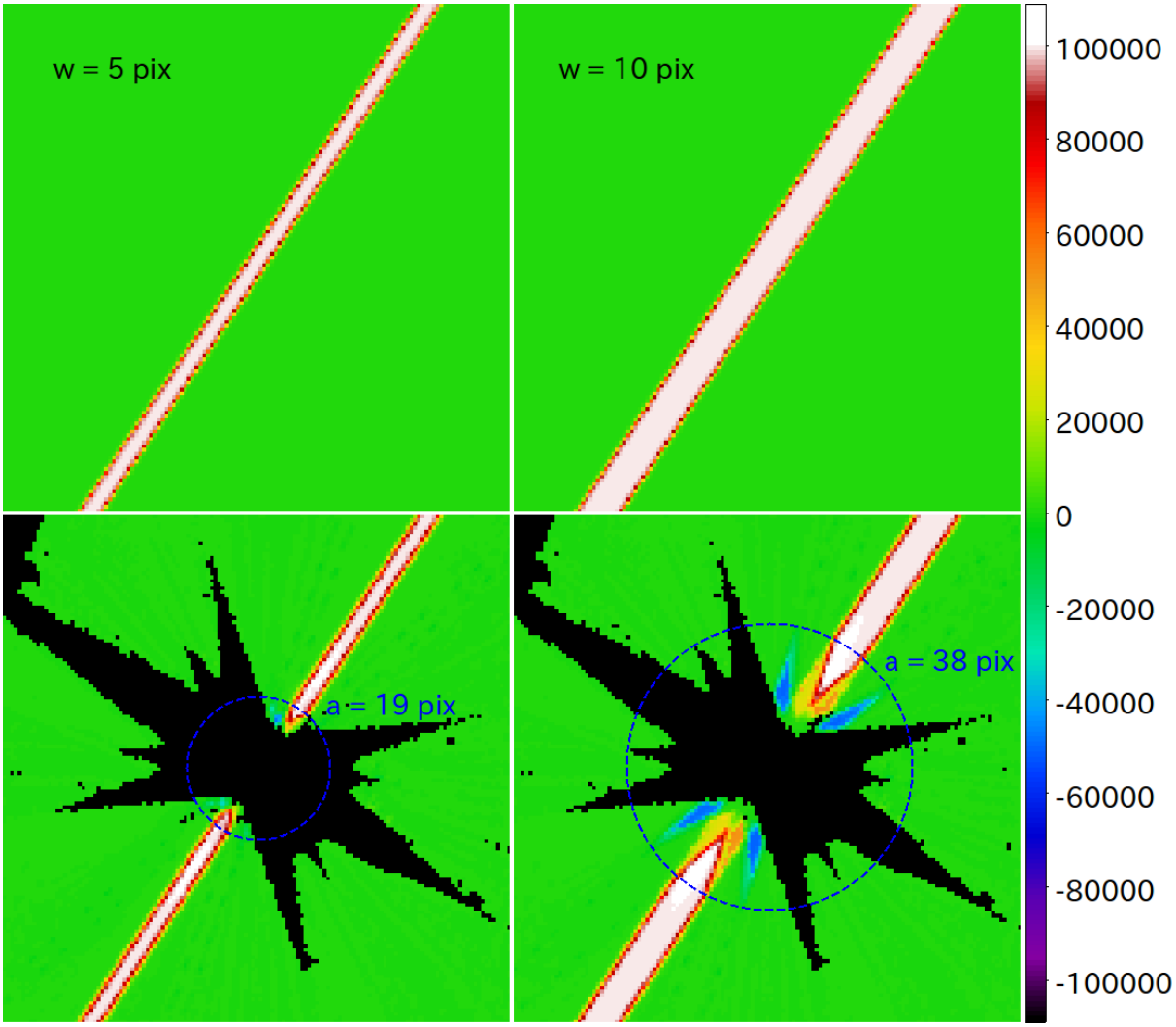

Figure 4: Artificial disk (top panels) and simulation results of self-subtraction (bottom panels). In the left and right panels, the disk width w is 5 pixels and 10 pixels, respectively. The 100000-levels intensity is the artificial disk brightness. The black region covers the spider patter or the saturated pixels. The blue-dashed circle represents the projected distance affected by self-subtraction.

3.4 Model fitting

3.4.1 Disk model

The disk geometry was probed by an annulus disk model. The dust density is assumed to follow inner/outer power-law slopes in the radial direction and a Gaussian distribution in the vertical direction. The disk thickness increases proportionally to the radius. The density distribution is the function of the radius r and height h:

$$\rho_{r,h} \propto \frac{1}{\sqrt{\left(\frac{r}{R_{\rm d}}\right)^{2q_{\rm in}} + \left(\frac{r}{R_{\rm d}}\right)^{2q_{\rm out}}}} \exp\left(\frac{h^2}{2\left(\sigma_h \times \frac{r}{R_{\rm d}}\right)^2} \right) \tag{7}$$

(Augereau et al. 1999), where $R_{\rm d}$ is the ring radius and σ_h is the vertical scale height at $r = R_{\rm d}$. The indices $q_{\rm in}$ and $q_{\rm out}$ (both positive) are the inner and outer power-law slopes, respectively. We inclined this model disk at an inclination angle i (relative to the face-on view) and varied the location of the disk center. Assuming that the dust-scattered light follows the Henyey-Greenstein phase function, the surface brightness $F(r, h)$ is calculated as

$$F(r,h) = A \times \frac{1}{d^2} \times \rho_{r,h} \times \frac{1 \quad g^2}{(1 + g^2 \quad 2g\cos\alpha)^{3/2}}, \tag{8}$$

where A is the scaling factor, d is the distance from the star, g is the asymmetry parameter, and α is the scattering angle. For disks with extremely symmetric surface brightness, such as HD 15115 and HD 61005 disks, we varied the scaling factor A on each side of the disk.

3.4.2 Fitting method

To examine the fitness between the observation and the model, we projected the model disk onto a two-dimensional plane (x, y) and probed the disk geometry. The residual sum of squares between the observation and model images was calculated as follows:

$$\chi^2 = \sum_{x,y} \left(\frac{I_{\rm obs}(x,y) \quad I_{\rm mod}(x,y)}{\sigma_{\rm obs}(x,y)} \right)^2 . \tag{9}$$

The error $\sigma_{\rm obs}(x, y)$ was estimated as the standard deviation of the pixel values in the nearby sky, excluding the disk. The model that minimized the χ^2 was assumed as the best-fit model. We refer to this fitting method as *photometric fitting*.

Figure 5 demonstrates the model fitting of HD 202628. The residual map is almost devoid of disk components, indicating that the modeled disk well reproduces the observed disk image.

3.4.3 Comparison with disk structure fitting

The fitting method described in Section 3.4.2 (photometric fitting) differs from the one executed in paper 1. In paper 1, we measured the PA, surface brightness, and FWHM of the HD 15115 disk. We then calibrated the disk surface brightness and FWHM by simulating the self-subtraction of artificial disks. The model disk whose position, brightness, and width best matched the calibrated disk was considered as the best model. We refer to this fitting method as *disk structure fitting*.

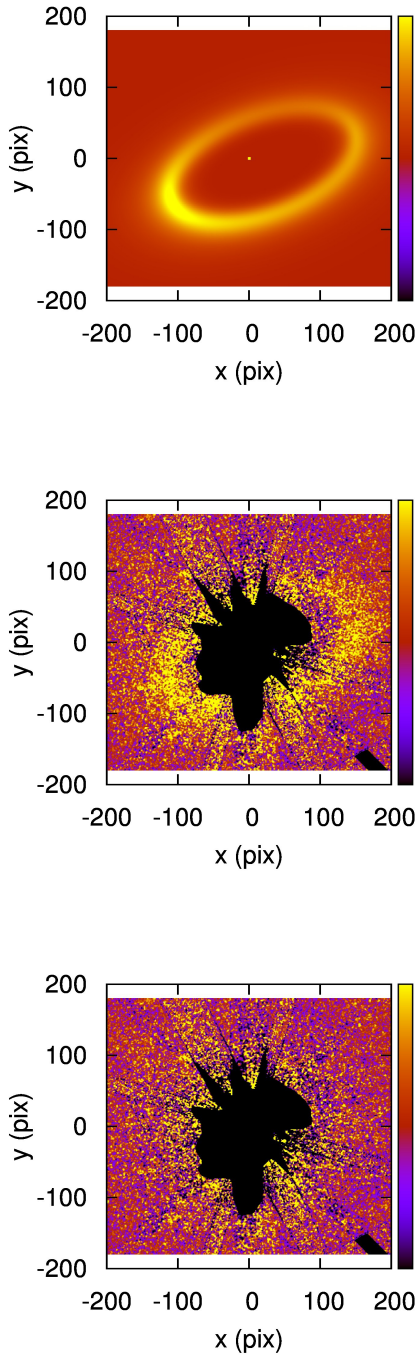

Figure 5: Example of model fitting (HD 202628). Top: model disk. Middle: observation. Bottom: residual map (observation - model). The coordinate $(x, y) = (0, 0)$ represents the star position.

We now compare the photometric and disk structure fittings of HD 15115. Because we cannot derive $q_{\rm in}$ in the disk structure fitting, we set $q_{\rm in} =$ √, i.e.,

$$\begin{cases} \rho_{r,h} \propto \left(\frac{r}{R_{\rm d}}\right)^{q_{\rm out}} \exp\left(-\frac{h^2}{2\left(\sigma_h \times \frac{r}{R_{\rm d}}\right)^2}\right) & (\text{if } r \sim R_{\rm d}) \\ \rho_{r,h} = 0 & (\text{if } r < R_{\rm d}) \end{cases} . \quad (10)$$

Table 3 lists the HD 15115 disk parameters obtained by each fitting method. The two methods yielded similar $R_{\rm d}$, g,i and disk PA, but very different values of $q_{\rm out}$ and $\sigma_{\rm h}$. Especially, the $\sigma_{\rm h}$s differed by more than one order of magnitude. These disparities might be caused by the calibration of disk surface brightness and width by self-subtraction. As the self-subtraction was not corrected in the photometric fitting, the $\sigma_{\rm h}$ and $q_{\rm out}$ values obtained by this method might be unreliable, especially when the self-subtraction is large.

Table 3: Disk parameters of HD 15115 obtained by photometric fitting and disk structure fitting

	$R_{\rm d}$ (AU)	$q_{\rm in}$	$q_{\rm out}$	$\sigma_{\rm h}$ (AU)	g	i (degree)	disk PA (degree)
Photometric fitting	86.0	(√)	2.8	2.6	0.65	86.3	278.6
Disk structure fitting	87.2	>30	4.8	<0.1	0.50	87.5	278.5

4 Results

In this study, we obtained the disk parameters (R_d, σ_h, q_{in}, q_{out}, g, i, disk PA) of nine targets (see Table 4). Among these, the disk parameters of HD 141943 and HD 139664 have been reported for the first time. For each target, the errors in the parameters were computed as the 68% confidence levels satisfying $\chi^2 \geq \chi^2_{min} + 1$, where χ^2_{min} is the minimum of χ^2. Defining χ_{min}/ν as the reduced minimum chi-square, the number of degrees of freedom ν was obtained by

$$\nu = N_{pix} \quad N_{par}, \tag{11}$$

where N_{pix} is the number of pixels in the image, excluding the unused pixels (bad pixels, occulting masks, and other field stars), and N_{par} is the number of disk parameters. We also cited the disk parameters of 13 targets reported in previous studies. For almost all targets, R_d was determined to an accuracy of several AU (see Table 4).

4.1 Comparison with previous disk parameters

In this section, we compare our seven derived disk geometries with those reported in previous studies.

Using the same original data as ourselves, Buenzli et al. (2010) imaged the HD 61005 and obtained $R_d = 61.25 \oplus 0.85$ AU, $g \propto 0.3$, and $i = 84.3 \oplus 1^{\leq}$. These values slightly differ from our parameters ($R_d = 56$ AU, $g = 0.6$, and $i = 87^{\leq}$).

Krist et al. (2012) imaged the HD 202628 disk and visually fitted an inclined ellipse to the ring inner edge. They obtained an inner edge semimajor axis of 158 AU and an inclination of $61^{\leq}$. Their inner edge is not directly comparable to our R_d due to the different definitions. Meanwhile, our inclination equals that of Krist et al. (2012). Moreover, our g is consistent with the results of the disk demonstration ($0.15 < g < 0.25$) in Krist et al. (2012).

For the HD 207129 disk, Krist et al. (2010) obtained $R_d = 163$ AU and $i = 60 \oplus 3^{\leq}$. The R_d coincides with that obtained in this study, but their i is slightly smaller.

Stapelfeldt et al. (2007) reported the disk radius of HD 10647 as 90 AU, which is $\propto$7 AU larger than our derived disk radius.

Mazoyer et al. (2014) resolved the HD 15115 disk image and obtained $R_d \propto 90$ AU and $i = 86^{\leq}$. Both values almost coincide with our results. They also derived $g \propto 0.25$, which is smaller than our result.

For the Fomalhaut disk image, Kalas et al. (2013) obtained $R_d = 141.3 \oplus 0.4$ AU and $i = 66.0^{\leq} \oplus 0.2^{\leq}$. Again, these results are entirely consistent with those of our study.

Rodigas et al. (2015) resolved the HR 4796A disk image and obtained $R_d = 79$ AU, $i = 77^{\leq}$, $q_{in} = 19.6$, and $q_{out} = 6$. For the same disk, we obtained $R_d = 73$ AU, $i = 76^{\leq}$, $q_{in} = 36$, and $q_{out} = 4$. Clearly, the R_d, q_{in}, and q_{out} differ between the previous study and our study.

Although there are discrepancies in the disk parameters obtained by us and previous authors, we consider that these differences will not compromise the following discussion.

Table 4: Disk parameters

Targets	$R_{\rm d}$	$q_{\rm in}$	$q_{\rm out}$	$\sigma_{\rm h}$	g	i	disk PA	$\chi^2_{\rm min}/\nu$	Reference
TWA 7	40^{+10}_{8}	...	...	...	$0.15^{+0.85}_{0.15}$	25⊕25	59⊕150	...	(1)
AU Mic	35	1.5	2.5	0.77	0.7⊕0.1	88.5⊕1.5	128.6⊕0.2	...	(2), (3), (4)
TWA 25	78⊕17	...	...	...	0.6⊕0.3	75⊕6	336⊕8	...	(1)
HD 35650	54^{+5}_{14}	...	...	...	$0.7^{+0.1}_{0.5}$	89^{+1}_{4}	189⊕7	...	(1)
HD 92945	59.3	...	...	...	0.015⊕0.015	62.4⊕0.2	100⊕2	...	(5), (6)
HD 61005	56⊕0.4	...	1.05⊕0.04	1.39⊕0.03	0.606⊕0.006	86.96⊕0.04	68.97⊕0.03	1.00	This work
HD 107146	118	1.6⊕0.5	2.8⊕0.3	...	0.25⊕0.05	25⊕5	148⊕5	...	(5), (7)
HD 202628	170.5⊕1.2	10.5⊕0.7	3.05⊕0.15	15.56⊕1.24	0.237⊕0.007	60.55⊕0.35	305.35⊕0.3	1.56	This work
HD 377	86⊕15	...	...	...	0.4⊕0.4	85⊕5	227⊕4	...	(1)
HD 207129	165.4⊕1.1	18⊕2	10.05⊕0.45	6.6⊕0.8	0.018⊕0.018	66.4⊕0.4	122.05⊕0.25	1.32	This work
HD 10647	82.9⊕0.1	16.5⊕0.7	1.16⊕0.01	8.19⊕0.1	0.339⊕0.003	78.72⊕0.09	56.13⊕0.03	1.84	This work
HD 141943	104.4⊕0.2	22.5⊕1	2.53⊕0.02	3.83⊕0.05	0.646⊕0.006	86.32⊕0.04	326.24⊕0.02	1.88	This work
HD 15115	87.2⊕0.7	70.6⊕32.9	4.78⊕0.15	0.04⊕0.04	0.499⊕0.011	87.53⊕0.03	278.46⊕0.03	1.36	This work
HD 181327	90.5⊕1.1	7	3.7	...	0.3	28.5⊕2	101.2⊕4.6	...	(8)
HD 139664	88.6⊕0.8	4.4⊕0.3	6.16⊕0.26	12.56⊕0.15	0.247⊕0.027	87.11⊕0.35	255.94⊕0.1	1.48	This work
HD 115600	48^{+0}_{1}	$7.5^{+2.5}_{0}$	$7.5^{+0}_{2.5}$	3⊕2	0	79.5⊕0.5	24⊕0.5	...	(9)
HD 106906	56	...	4.5⊕0.3	5.09	0.6⊕0.1	85.3⊕0.2	104.35⊕0.35	...	(10), (11)
beta Pic	112⊕2	$4.7^{+0.5}_{0.2}$	$2.8^{+0.4}_{0.2}$	4.87	$0.635^{+0.006}_{0.004}$	$89.88^{+0.04}_{0.03}$	29.1⊕0.1	...	(12), (13)
HD 32297	110	10	6	2	0.5	88	227⊕0.3	...	(14), (15)
HD 131835	75^{+2}_{4}	...	$2.3^{+0.1}_{0.2}$	...	...	$75.1^{+0.8}_{0.9}$	241.4⊕0.4	...	(16)
Fomalhaut	141.8⊕0.1	35.1⊕0.4	15.92⊕0.13	1.62⊕0.04	0.27⊕0.002	66.73⊕0.02	336.48⊕0.02	1.78	This work
HR 4796A	72.6⊕0.1	36⊕3	4.18⊕0.03	3.9⊕0.12	0.039⊕0.004	75.58⊕0.08	27.02⊕0.04	1.10	This work

References

(1) Choquet et al. 2015; (2) Augereau and Beust 2006; (3) Fitzgerald et al. 2007; (4) Krist et al. 2005; (5) Schneider et al. 2014; (6) Golimowski et al. 2011; (7) Ardila et al. 2004; (8) Stark et al. 2014; (9) Currie et al. 2015; (10) Kalas et al. 2015; (11) Lagrange et al. 2015; (12) Ahmic et al. 2009; (13) Apai et al. 2015; (14) Currie et al. 2012b; (15) Boccaletti et al. 2012; (16) Hung et al. 2015

4.2 Disk radius versus stellar age

Figure 6 plots the disk radius R_d against the stellar age t. The R_d trends slightly upward with increasing age. On a log-log plot of this relation, the correlation coefficient is 0.57. The uncertainties in some targets are large because the ages largely depend on their estimation methods. The following figures are R_d versus t plots for different age estimations: moving groups identified in proper motions (Figure 7), isochrones of the stellar evolution model in HR diagrams (Figure 8), strengths of the H and K lines of Ca II (which indicate chromospheric activity) (Figure 9), and lithium abundance (Figure 10). Regardless of the method used, R_d is an increasing function of age. This feature will be discussed in Section 5.2.

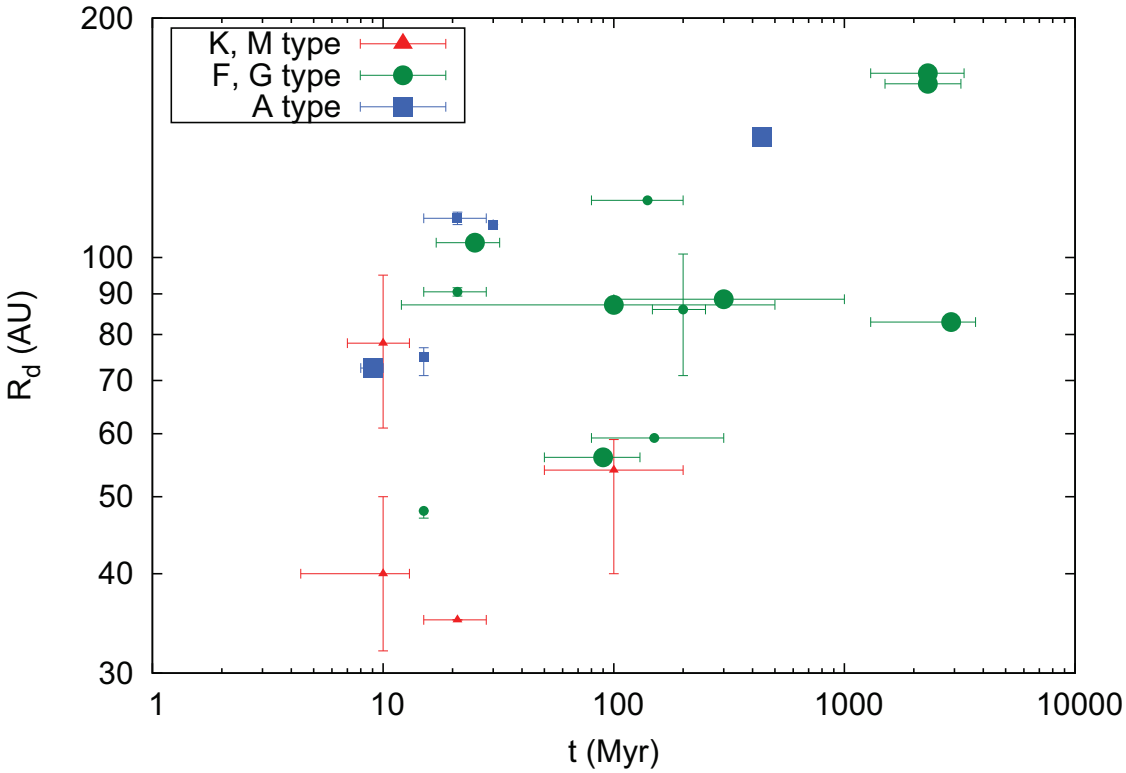

Figure 6: R_d versus t. The red triangles, green circles, and blue squares represent K or M-, F or G-, and A-type stars, respectively. Larger and smaller symbols indicate the disk radii derived by our model fitting and referred from previous studies, respectively. R_d apparently increases with t.

4.3 Disk radius versus stellar mass

Figure 11 plots the the disk radius R_d as a function of stellar mass $M_{\pm}$. Most of the stellar masses were estimated by fitting the evolutionary tracks to the HR diagram. Here, the evolutionary tracks were determined from pre-main-sequence stars evolutional tracks Baraffe et al. (1998), the Yale rotational evolution code Guenther et al. (1992), and the Padova stellar evolution code Bertelli et al. (2008). The mass of TWA 25 was derived from the temperature-mass relation (Mann et al.

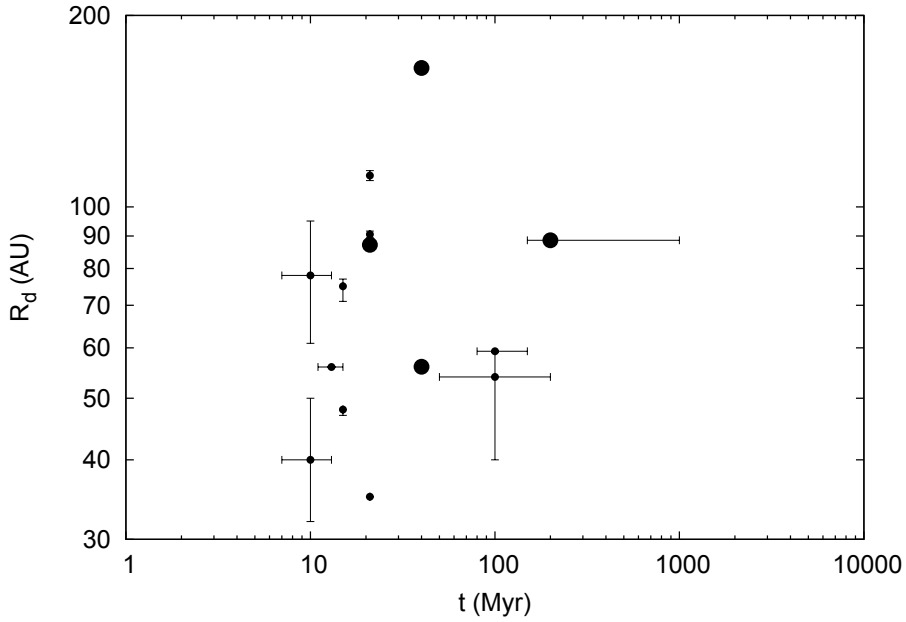

Figure 7: $R_{\rm d}$ versus t determined by the identification of moving groups. Larger and smaller symbols indicate the disk radii derived by our model fitting and referred from previous studies, respectively.

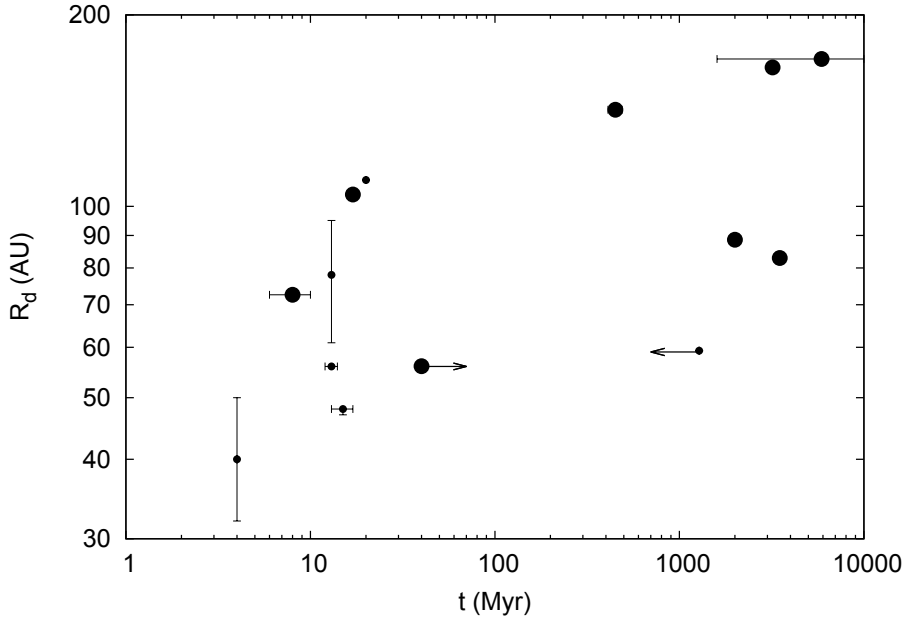

Figure 8: $R_{\rm d}$ versus t plot determined from isochrones of the evolution tracks. Larger and smaller symbols indicate the disk radii derived by our model fitting and referred from previous studies, respectively

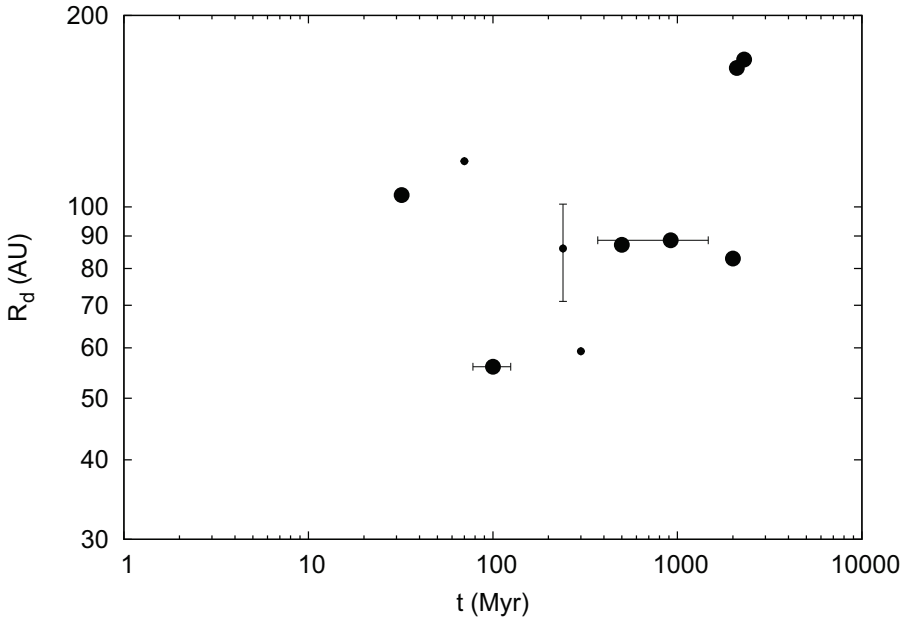

Figure 9: R_d versus t plot determined from the H and K lines of Ca II. Larger and smaller symbols indicate the disk radii derived by our model fitting and referred from previous studies, respectively.

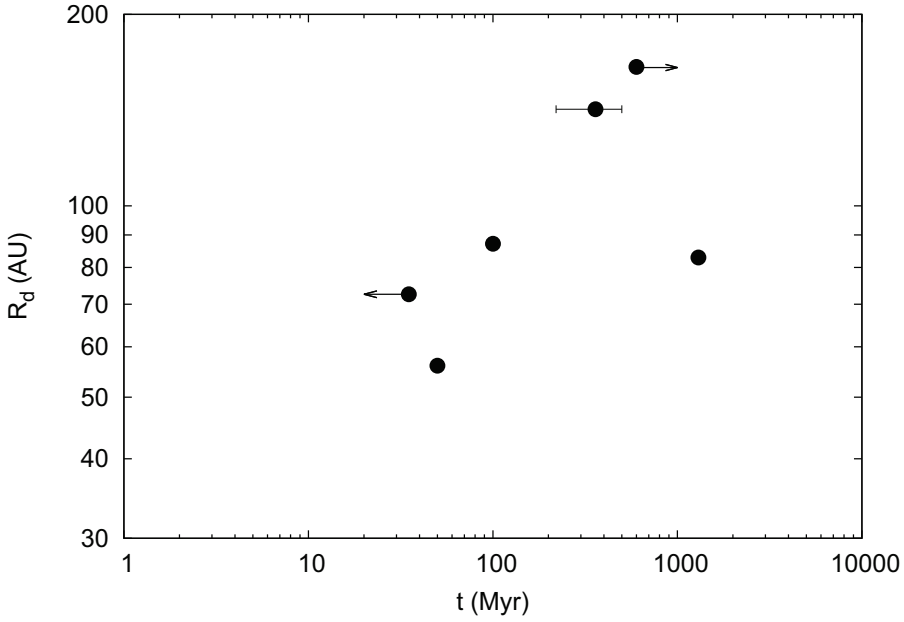

Figure 10: R_d versus t plot determined by the lithium abundances. All disk radii were derived by our model fitting.

2013). The mass of HD 141943 was estimated from the V-band mass-luminosity relation (Xia and Fu 2010). On a log-log plot of R_d versus $M_{\pm}$, the correlation coefficient was 0.51. Figure 11 reveals

an upward trend of $R_{\rm d}$ with increasing mass, although the correlation is weak. This feature will be discussed in Section 5.2.

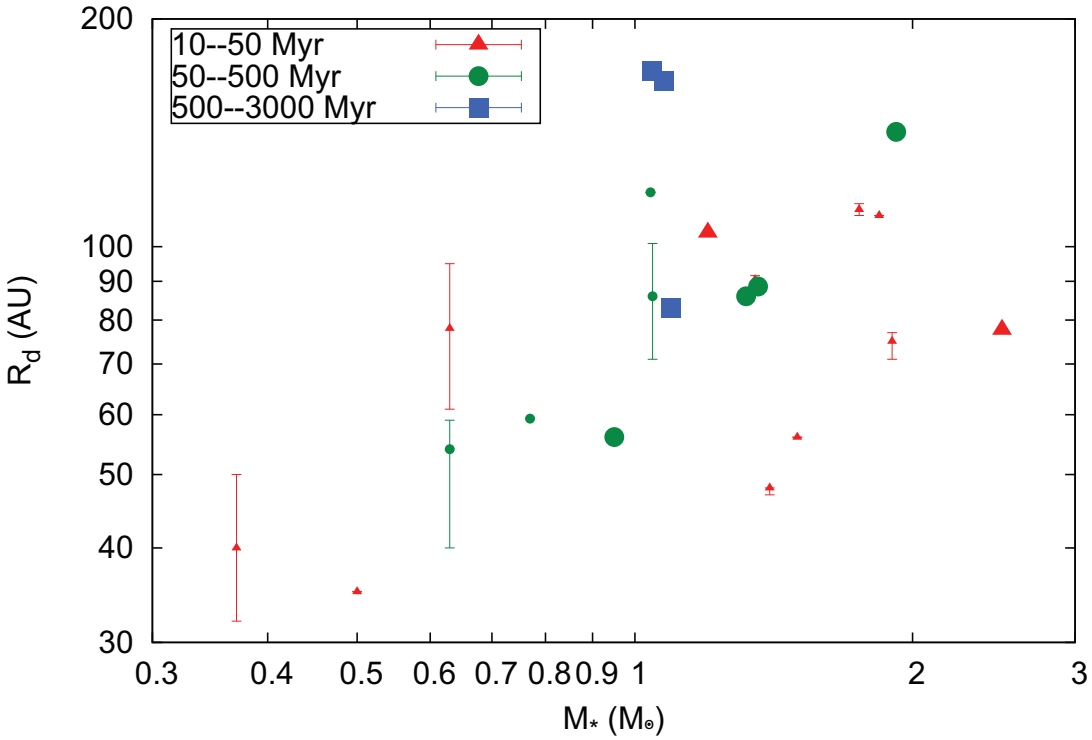

Figure 11: $R_{\rm d}$ versus $M_{\pm}$. The red triangles, green circles, and blue squares represent stellar ages of 10–50, 50–500, and 500–3000 Myr, respectively. Larger and smaller symbols indicate the disk radii derived by our model fitting and referred from previous studies, respectively. $R_{\rm d}$ appears to increase with $M_{\pm}$.

4.4 Comparison with SED results

To check consistency between our derived disk radii and the SED results, we compared the disk radii with the SED disk radii derived by Chen et al. (2014), who analyzed 571 debris disk candidates with the *Spitzer Space Telescope* Infrared Spectrograph (IRS) and Multiband Imaging Photometer for *Spitzer* (MIPS) data and fitted them to a one- or two-temperature blackbody model. The two-temperature model assumes that one system has two disks (a hot disk and a cold disk). In Figures 12 and 13, we plot our derived radii and the SED disk radii with respect to t and $M_{\pm}$, respectively. In both figures, the disk radii are located in the middle of the cold disk distribution, and are within the variation of the radii derived from the one-temperature model.

Figure 14 plots the SED disk radii $R_{\rm d,SED}$ versus the direct imaging disk radii $R_{\rm d,DI}$ for the common targets in the present study and Chen et al.'s (2014) study. The $R_{\rm d,SED}$s are nearly evenly dispersed around $R_{\rm d,DI}$ by a factor of $\propto 3$. The average and variance of the ratio of these two radii

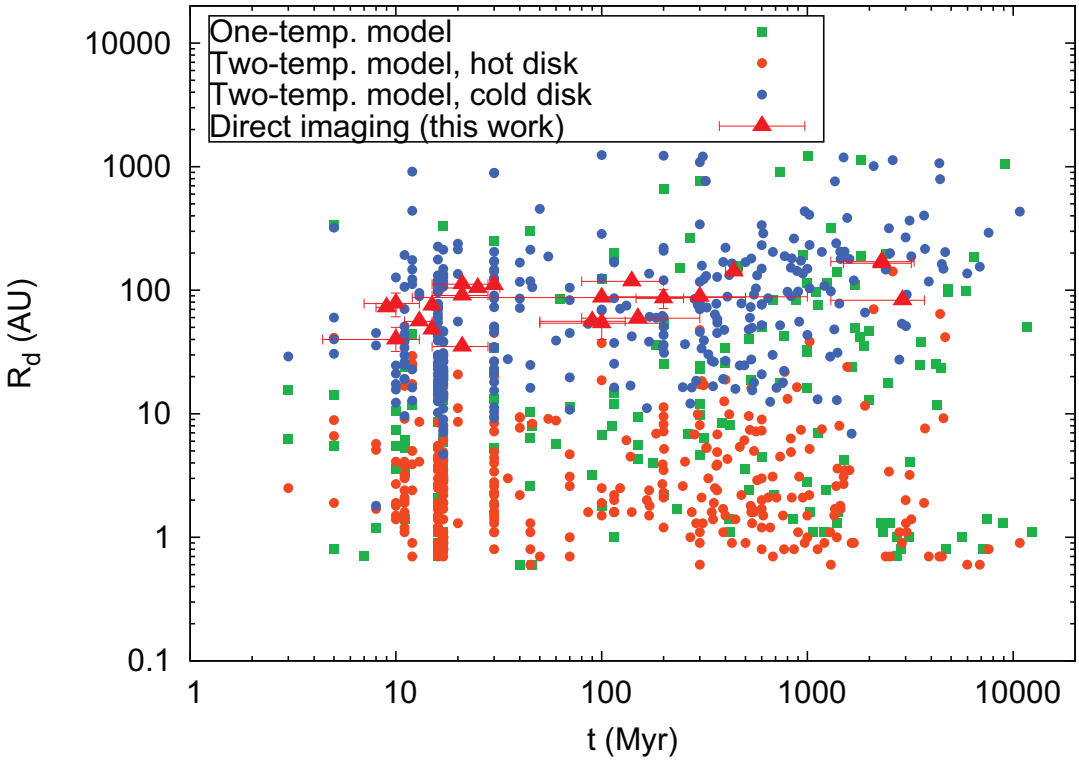

Figure 12: $R_{\rm d}$ versus t plot using our radii and the SED disk radii from Chen et al. (2014). The green squares are the fittings to the one-temperature model, and the orange and blue circles represent the hot and cold disks fitted by the two-temperature model, respectively. The red triangles represent the disk radii obtained by direct imaging. These radii are located within the ranges f the cold disks and the one-temperature model disks.

were computed as $\overline{R_{\rm d,SED}/R_{\rm d,DI}} = 1.4^{+0.7}_{0.6}$ (95 % confidence interval). The $R_{\rm d,SED}$ are slightly larger than $R_{\rm d,DI}$.

4.5 Parameter dependence of disk radius

The disk radius was found to be correlated with stellar age and mass. To quantitatively evaluate the disk radius dependence, we calculated the disk radius as

$$R_{\rm d} \propto t^p M_{\pm}^q \,. \tag{12}$$

We then derived the age index p and the stellar mass index q from the observational results. $M_{\pm}$ was completely uncorrelated with t (correlation coefficient: -0.006, Figure 15). Equation (12) was linearized by taking the logarithm of both sides. Inserting the known values of $\log R_{\rm d}$, $\log t$, and $\log M_{\pm}$ into this linearized equation, we obtained $p = 0.13 \oplus 0.07$ and $q = 0.45 \oplus 0.28$ (95 % confidence level) by multiple regression analysis.

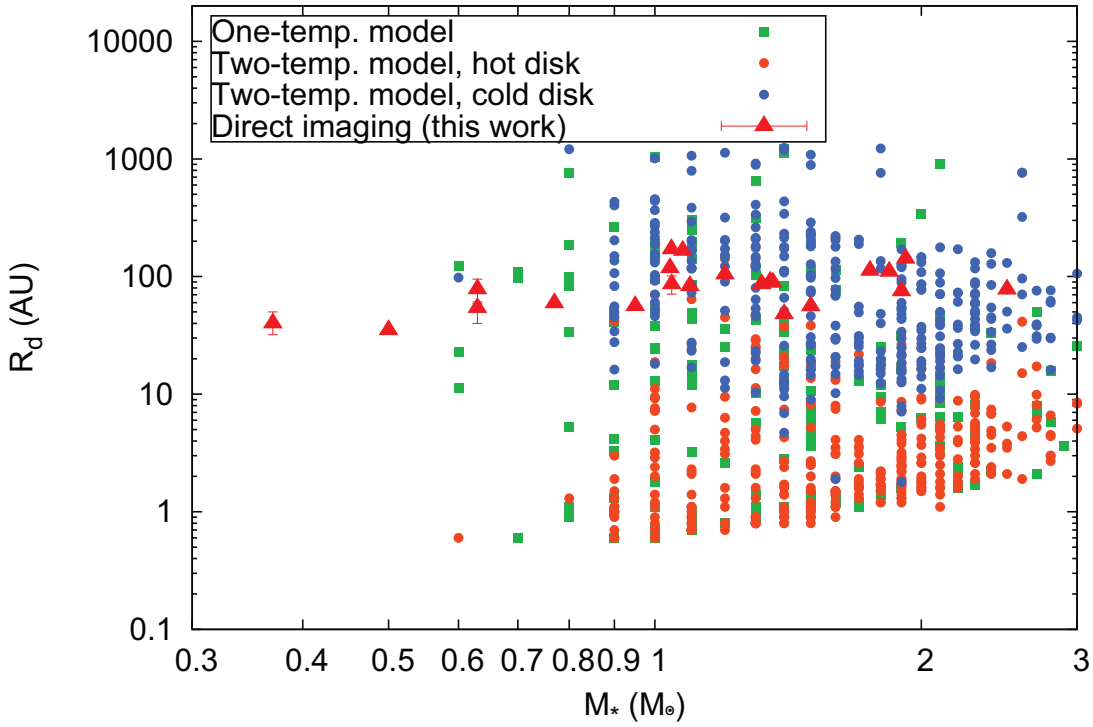

Figure 13: $R_{\rm d}$ versus $M_{\pm}$ plots using our radii and the SED disk radii from Chen et al. (2014). The green squares are the fittings to the one-temperature model. The orange and blue circles represent the hot and cold disks fitted by the two-temperature model, respectively. The red triangles represent the disk radii obtained by direct imaging. For $M_{\pm} \sim 0.6 M_{\odot}$, the direct imaging radii are located within the ranges of the cold disks and the one-temperature model disks.

4.6 Other disk parameters

We also investigate the other disk parameters: vertical thickness σ_h, density slopes $q_{\rm in}$ and $q_{\rm out}$, scattering asymmetry parameter g, inclination i, and disk PA. Table 5 shows the correlation coefficients between each parameter and the stellar age or mass. When calculating these coefficients, we took the log of the parameters (except for g, i, and disk PA). When calculating the σ_h correlation coefficients, we excluded the doubtful value of HD 15115 ($\sigma_h < 0.1$ AU).

Table 5: Correlation coefficients

	$\log R_{\rm d}$	$\log \sigma_{\rm h}$	$\log q_{\rm in}$	$\log q_{\rm out}$	g	i	disk PA
$\log t$	0.57	0.51	0.17	0.06	-0.27	-0.01	0.20
$\log M_{\pm}$	0.51	0.24	0.54	0.38	-0.19	0.25	0.04

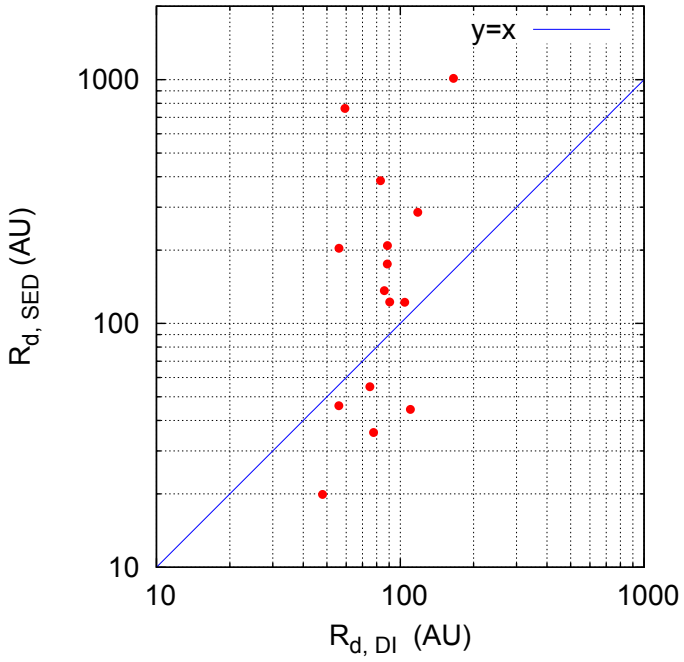

Figure 14: R_d relation between visible/NIR direct imaging (this study) and SED (Chen et al. 2014). The blue line is the 1:1 correspondence line between the two disk radii.

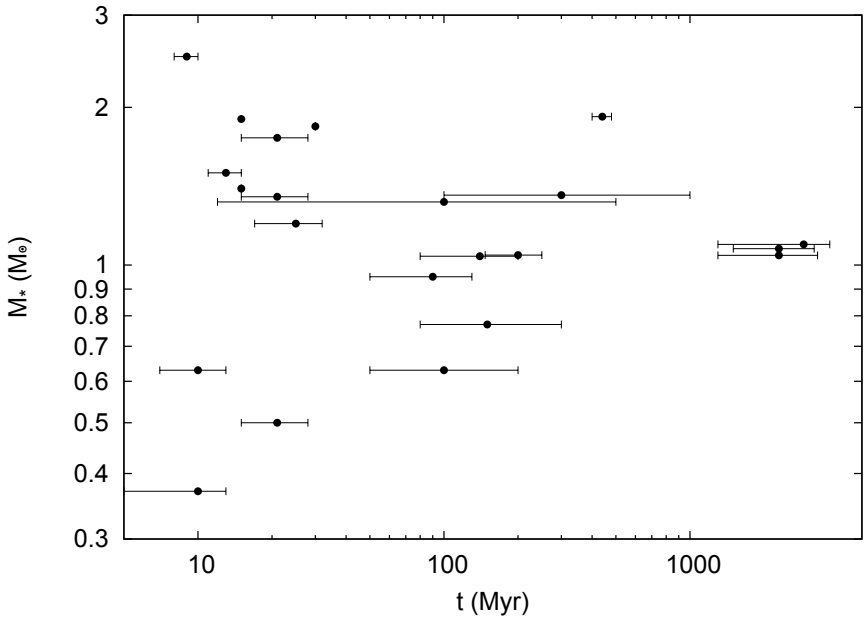

Figure 15: Stellar age versus mass for the targets investigates in this study. The age and mass are completely uncorrelated.

4.6.1 Vertical thickness

Ignoring the suspicious thickness of HD 15115 (σ_h <0.1 AU), the $\log \sigma_{\rm h}$ and $\log t$ were weakly correlated (correlation coefficient: 0.51). Figure 16 plots the vertical thickness $\sigma_{\rm h}$ as a function of t. Meanwhile, the $\log \sigma_{\rm h}$ and $\log M_{\pm}$ were very weakly correlated (correlation coefficient: 0.24).

The age and mass indices were examined by multiple regression analysis as described in Section 4.5. We discarded the anomalous disk thickness of HD 15115. The age and mass indices were $0.24 \oplus 0.23$ and $0.75 \oplus 1.16$, respectively (95 % confidence level).

4.6.2 Density slopes

Both $q_{\rm in}$ and $q_{\rm out}$ were correlated with $M_{\pm}$ (correlation coefficients 0.54 and 0.38, respectively). Figures 17 and 18 plot $q_{\rm in}$ and $q_{\rm out}$ as functions of $M_{\pm}$, respectively. Conversely, $q_{\rm in}$ and $q_{\rm out}$ were uncorrelated with t (correlation coefficients 0.17 and 0.06, respectively).

4.6.3 Scattering asymmetry parameter

There is a weak negative correlation between $\log g$ and $\log t$ (correlation coefficient: -0.27). Figure 19 plots the scattering asymmetry parameter g as a function of t. We observed that the upper margin declines with increasing t.

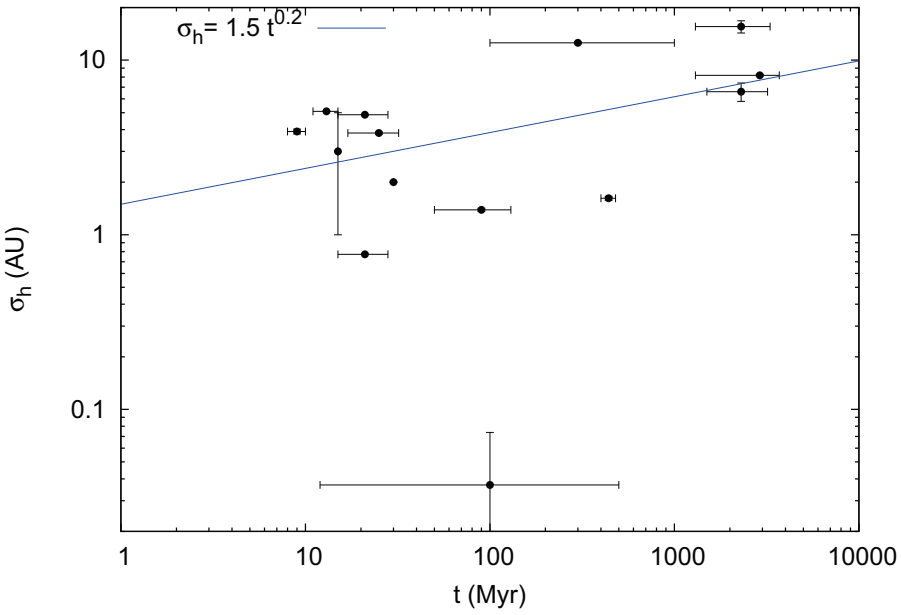

Figure 16: σ_h versus t. The blue line is the best-fit line (excluding HD 15115; σ_h <0.1 AU).

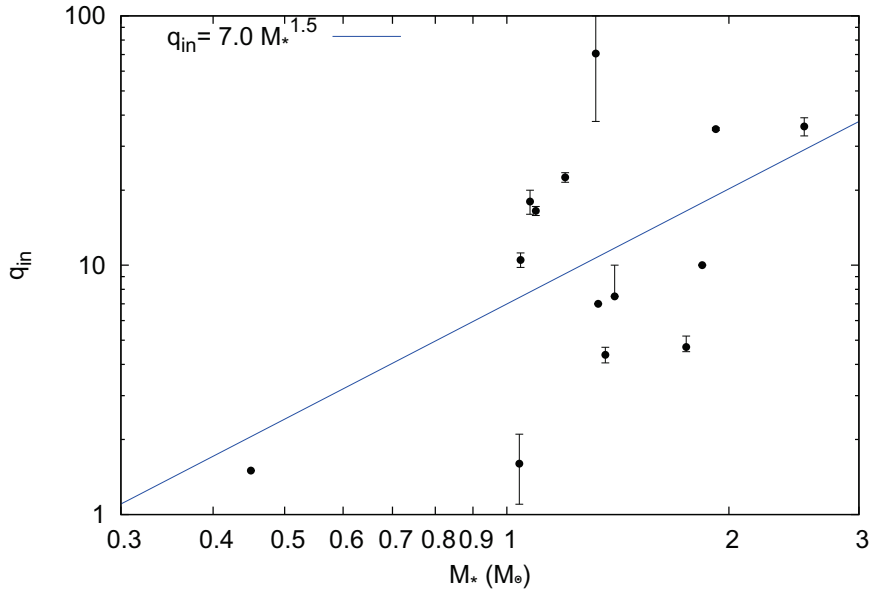

Figure 17: $q_{\rm in}$ versus $M_{\pm}$. The blue line is the best-fit line.

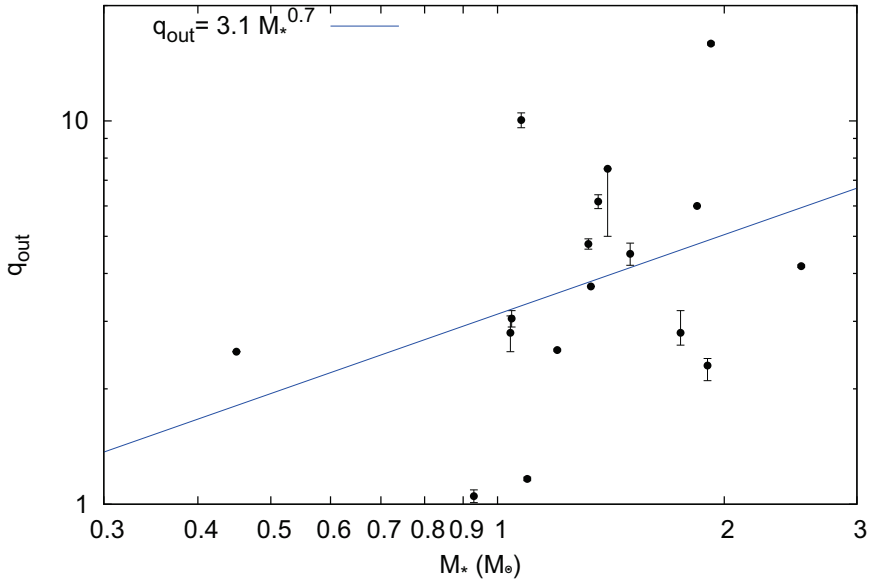

Figure 18: q_{out} versus $M_{\pm}$. The blue line is the best-fit line.

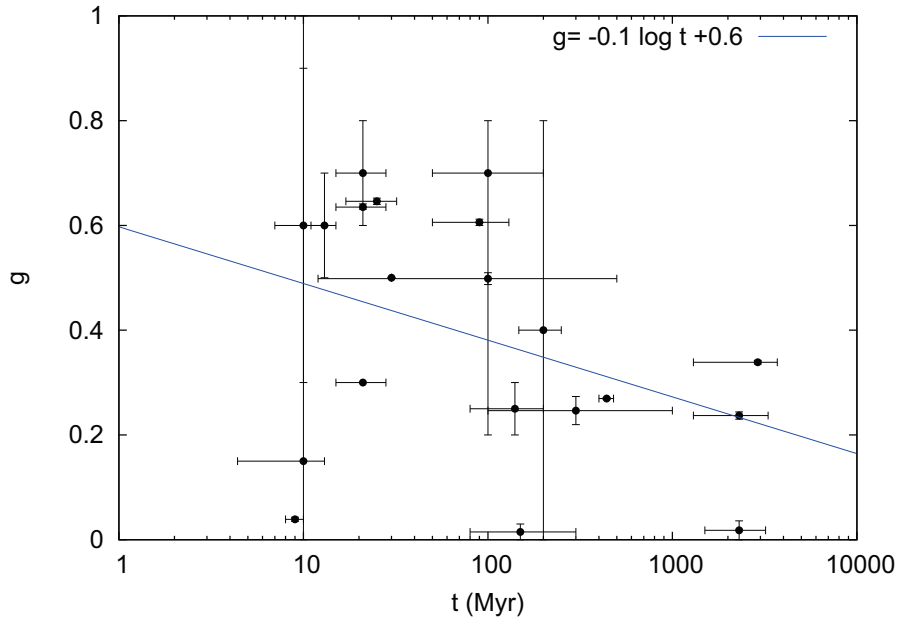

Figure 19: g versus t. The blue line is the best-fit line.

5 Discussion

5.1 Are debris disks really optically thin?

In Section 3.4.1, we assumed that debris disks are optically thin. To validate or refute this assumption, we calculate the optical depth of the debris disk.

First, we estimate the radial optical depth, τ_r. We assume that the grains are uniformly sized with radius s and are distributed at a distance d from the star. In addition, we set the absorption efficiency as $Q_{\rm abs} = 1$. At radiative equilibrium, the stellar and dust luminosities, $L_{\pm}$ and $L_{\rm dust}$, respectively, are related as

$$\sum_{s=s_{\rm min}}^{s_{\rm max}} \frac{L_{\pm}}{4\pi d^2} \pi s^2 N(s) = L_{\rm dust} \ , \tag{13}$$

where $N(s)$ is the number of grains of radius s. Thus, the fractional luminosity

$$\frac{L_{\rm dust}}{L_{\pm}} = \sum_{s=s_{\rm min}}^{s_{\rm max}} \frac{N(s)\pi s^2}{4\pi d^2} \tag{14}$$

represents the area ratio of the total cross-section of the grains to a spherical shell of radius d. When the grain distribution is spherically homogeneous, the fractional luminosity corresponds to the radial optical depth. When a debris disk with ring radius $R_{\rm d}$ is vertically displaced by σ_h from the mid-plane, the grains on the surface of the sphere are considered to accumulate in the mid-plane belt. The radial optical depth of the debris disk, τ_r, is then simply written as

$$\tau_r = \frac{4\pi R_{\rm d}^2}{2\pi R_{\rm d} * 2\sigma_h} \frac{L_{\rm dust}}{L_{\pm}} = \frac{R_{\rm d}}{\sigma_h} \frac{L_{\rm dust}}{L_{\pm}} \ . \tag{15}$$

Next, we calculate the optical depth $\tau_{\rm ans}$ at the disk ansa, which is optically thickest in the edge-on view. We assume a ring disk (radius: $R_{\rm d}$, width: $\Delta R_{\rm d}$) of uniform spatial density. The maximum length of the dense region along the line of sight reaches $\overline{8R_{\rm d}\Delta R_{\rm d}}$ (Figure 20). Thus, $\tau_{\rm ans}$ is calculated as

$$\tau_{\rm ans} = \frac{\overline{8R_{\rm d}\Delta R_{\rm d}}}{\Delta R_{\rm d}} \tau_r = \sqrt{\frac{8R_{\rm d}}{\Delta R_{\rm d}}} \frac{R_{\rm d}}{\sigma_h} \frac{L_{\rm dust}}{L_{\pm}} \ . \tag{16}$$

According to this equation, the optical depth at the disk ansa is enhanced by narrow width and/or vertical thinness.

In previous SED observations, $L_{\rm dust}/L_{\pm}$ (= $L_{\rm IR}/L_{\pm}$; the excess luminosity over the stellar luminosity at all infrared wavelengths) was determined as $\lesssim 10^{-3}$ (Table 6). In addition, even in a very narrow ring systems such as Fomalhaut, the $R_{\rm d}/\Delta R_{\rm d}$ never exceeds $\propto$10. To satisfy $\tau_{\rm ans} > 1$, the vertical thickness should be $\sigma_h/R_{\rm d} < 0.001$, which is unrealistic (Figure 21, Table 6). Thus debris disks should be optically thin.

5.2 Origin of stirring

Three hypotheses of stirring mechanisms have been proposed, namely stellar flyby, planetary stirring, and self-stirring. This section discusses the feasibility of each mechanism.

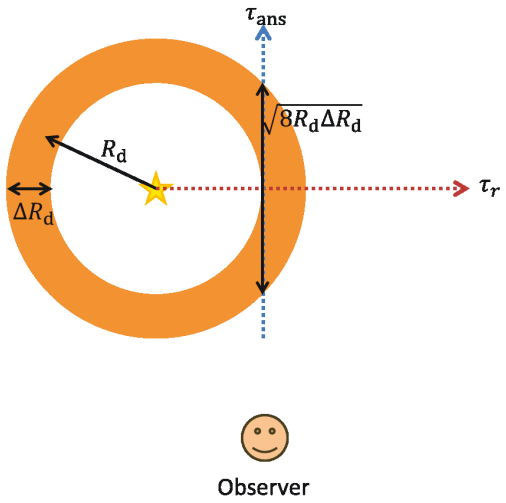

Figure 20: A toy disk model. $\sqrt{8R_d\Delta R_d}$ is the maximum distance along the disk.

Table 6: Fractional luminosities and aspect ratios of debris disks

Target	$L_{IR}/L_{\pm}$ ($*10^{-4}$)	σ_h/R_d	Reference of $L_{IR}/L_{\pm}$
TWA 7	22.0	···	Choquet et al. (2015)
AU Mic	3.6	0.022	Rhee et al. (2007)
TWA 25	···	···	···
HD 35650	1.8	···	Choquet et al. (2015)
HD 92945	4.9	···	Chen et al. (2014)
HD 61005	14.0	0.025	Chen et al. (2014)
HD 107146	4.2	···	Chen et al. (2014)
HD 202628	1.4	0.091	Krist et al. (2012)
HD 377	2.0	···	Choquet et al. (2015)
HD 207129	0.6	0.040	Chen et al. (2014)
HD 10647	1.9	0.099	Chen et al. (2014)
HD 141943	1.1	0.037	Chen et al. (2014)
HD 15115	3.3	0.0004	Chen et al. (2014)
HD 181327	8.3	···	Chen et al. (2014)
HD 139664	0.5	0.142	Chen et al. (2014)
HD 115600	17.0	0.063	Chen et al. (2014)
HD 106906	4.6	0.091	Chen et al. (2014)
beta Pic	26.4	0.043	Rhee et al. (2007)
HD 32297	38.0	0.018	Chen et al. (2014)
HD 131835	15.0	···	Chen et al. (2014)
Fomalhaut	0.8	0.011	Rhee et al. (2007)
HR 4796A	44.3	0.054	Rhee et al. (2007)

5.2.1 Stellar flyby

When a star closely encounters a planetary system, its gravity initiates stirring of the planetesimals (Kenyon and Bromley 2002). The debris disk formed by a stellar flyby disappears in $\lesssim 1$ 10 Myr, less than the timescale of stellar evolution. However, in our results, the disk radii approximately double over 10–1,000 Myr. This observation cannot be explained by the stirring mechanism of stellar flyby. Moreover, in field stars, a stellar approach within 500 AU occurs once per 10 Gyr (Wyatt 2008). Thus, debris disks are unlikely to be formed by the stellar flyby mechanism.

5.2.2 Planetary stirring

A Jupiter-mass planet can stir planetesimals by secular perturbation. We assume that the system produces dusts at $r = R_{\rm d}$ at a stellar age of $t = t_{\rm cross}$. We also suppose that the dusts are not radially shifted by the Poyinting-Robertson drag or radiation pressure. Under these assumptions, Equation (2) can be rearranged to yield

$$R_{\rm d} \propto t^{2/9} M_{\pm}{}^{1/9} . \tag{17}$$

Although $R_{\rm d}$ can vary by planet mass and orbital elements, Equation (17) indicates that, overall, $R_{\rm d}$ increases with stellar age and decreases with stellar mass.

By multiple regression analysis, the stellar age and mass indices are determined as $p = 0.13 \oplus 0.07$ and $q = 0.45 \oplus 0.28$, respectively. The observed age dependence is consistent with the theory. The positive mass dependence, however, is inconsistent with the theory.

As $R_{\rm d}$ can depend on the planet mass and orbiting elements, the planetary stirring model cannot be ruled out at present. Next, we examine individual debris disks containing detected planets (namely, beta Pic, HD 10647, and HD 106906).

The planet in the beta Pic system has a mass of $11 \oplus 5$ M_J (Snellen et al. 2014) and a semi-major axis $a_{\rm p}$ of $9.2^{+0.4}_{1.5}$ AU with an eccentricity $e_{\rm p}$ below 0.26 (Millar-Blanchaer et al. 2015). Inserting these parameters into Equation (2), we obtain $t_{\rm cross} \propto 100$ Myr at $r = R_{\rm d} = 112$ AU. This crossing time is one order of magnitude larger than the age of beta Pic ($\propto 21$ Myr). Thus, the planetary stirring model cannot explain the observed disk radius. However, the main disk of beta Pic encloses an inner disk (Heap et al. 2000) with a radius of 60–70 AU (Ahmic et al. 2009). The crossing time at this location is $\propto 10$ Myr, which roughly matches the stellar age. Hence, dust production can occur by planetesimal stirring in the inner disk of beta Pic b.

HD 10647 harbors an $M_{\rm p} \sin i = 0.93 \oplus 0.18$ M_J planet orbiting at $a_{\rm p} = 2.03 \oplus 0.15$ AU with $e_{\rm p} = 0.1 \oplus 0.01$ (Butler et al. 2006). Assuming that the planet's inclination equals the disk inclination $i = 78.7^{\leq}$, the planetary mass is obtained as $M_{\rm p} = 0.95 \oplus 0.18 M_J$. Inserting these parameters into Equation (2), we obtain $t_{\rm cross} = 30$–40 Gyr at $r = R_{\rm d} = 83$ AU. Again, this crossing time is one order of magnitude larger than the stellar age (1.3–3.7 Gyr). Therefore, the planetary stirring model is not supported by the debris disk HD 10647 b.

HD 106906 hosts an external $11 \oplus 2$ M_J planet (Bailey et al. 2014). The planet is located at a projected separation of 654 AU with a projected position of $23^{\leq}$ relative to the disk PA (Kalas et al. 2015). As the orbital parameters are not known, we cannot estimate $t_{\rm cross}$ at the disk radius (56 AU). However, given the huge separation and high inclination from the disk, HD 106906 b is unlikely to have formed under secular perturbation. Assuming that HD 106906 b was gravitationally scattered in the past, this system might harbor another massive planet that perturbs the orbits of the

planetesimals. The possibility of planetary stirring in the HD 106906 system requires verification by additional deep observations.

5.2.3 Self stirring

Pluto-sized objects can also stir the orbits of planetesimals. In this scenario, we assume that dust is immediately produced after the formation of a 1000 km object, and does not radially shift under Poyinting-Robertson drag or radiation pressure. Under these assumptions, Equation (3) can be rearranged as

$$R_{\rm d} = 50 x_m^{1.15/3} \left(\frac{t}{100\ {\rm Myr}}\right)^{1/3} \left(\frac{M_{\pm}}{M_{\circ}}\right)^{1/2} \ {\rm AU}. \tag{18}$$

Equation (18) infers that the disk radius increases with both stellar age and mass. In this equation, the mass index corresponds to our multiple regression analysis result, $q = 0.45$. Nevertheless, although the age index $p = 0.13$ is smaller than that predicted theoretically, the trend is consistent with the self-stirring model. Using Equation (18), we also estimate the x_m distribution (Figure 23). Fifteen of the 22 targets lie within $1 < x_m < 10$; the remaining 6 are located at $x_m \sim 10$. Figure 24 plots the mass-calibrated disk radius as a function of stellar age, assuming the self-stirring model. Half of the young stars (<30 Myr) exceed the $x_m = 10$ cutoff line, proposed by Mustill and Wyatt (2009) as the upper limit of disk gravitational stability in the protoplanetary stage. Therefore, the targets at $x_m > 10$ are unlikely to be formed by self-stirring and require modified self-stirring models or alternative hypotheses. Meanwhile, the other debris disks are consistent with the self-stirring scenario.

5.3 Interpretation of other disk parameters

In Section 4.6, we related the vertical thickness σ_h, inner/outer density slopes $q_{\rm in}/q_{\rm out}$, and scattering asymmetry parameter g to the stellar age t and mass $M_{\pm}$, and found correlations between these parameters and t or $M_{\pm}$. Below, we attempt to interpret these relations.

5.3.1 Collisional velocity

The vertical thickness σ_h possibly increases with t (Figure 16). The indices of σ_h and $R_{\rm d}$ (0.24⊕0.23 and 0.13 ⊕ 0.07, respectively) overlap, suggesting that the vertical thickness is limited by the disk radius. Figure 25 plots σ_h against $R_{\rm d}$ on a log-log scale. The best-fit line corresponds to the curve

$$\left(\frac{\sigma_h}{1\ {\rm AU}}\right) = 0.06 \left(\frac{R_{\rm d}}{1\ {\rm AU}}\right)^{0.9}, \tag{19}$$

indicating that the aspect ratio $\sigma_h/R_{\rm d}$ remains nearly constant.

From the aspect ratio, we can estimate the collisional velocity. The velocity dispersion is given by

$$v_{\rm rel} = \bar{6} \left(\frac{\sigma_h}{R_{\rm d}}\right) v_{\rm kep} \tag{20}$$

(Quillen et al. 2007), where $v_{\rm kep}$ is the orbital velocity of a circular orbit at $r = R_{\rm d}$. Figures 26 and 27 plot $v_{\rm rel}$ against t and $M_{\pm}$, respectively. The velocity dispersion appear to be independent of stellar mass and age.

5.3.2 Disk ring width

In Section 4.6.2, we showed that both $q_{\rm in}$ and $q_{\rm out}$ increase with the stellar mass. This result implies that more massive stars are associated with narrower ring widths. The ring widths were numerically obtained as

$$\Delta R_{\rm d} = r_{1/2}^{\rm out} \quad r_{1/2}^{\rm in} \,, \tag{21}$$

where $r_{1/2}^{\rm out}$ and $r_{1/2}^{\rm in}$ are the outer and inner radial locations, respectively, at which the radial density profile

$$\rho_r \propto \frac{1}{\sqrt{\left(\frac{r}{R_{\rm d}}\right)^{2q_{\rm in}} + \left(\frac{r}{R_{\rm d}}\right)^{2q_{\rm out}}}} \tag{22}$$

is half of the peak density. For targets with unavailable $q_{\rm in}$, we define the ring width as

$$\Delta R_{\rm d} = R_{\rm d}(2^{1/q_{\rm out}} \quad 1) \,, \tag{23}$$

that is, the FWHM of the radial profile of

$$\begin{cases} \rho_r \propto \left(\frac{r}{R_{\rm d}}\right)^{q_{\rm out}} & (\text{if } r \sim R_{\rm d}) \\ \rho_r = 0 & (\text{if } r < R_{\rm d}) \end{cases} . \tag{24}$$

The derived normalized ring widths $\Delta R_{\rm d}/R_{\rm d}$ approximately agree with the ring widths reported in Krist et al. (2012). Figure 28 plots $\Delta R_{\rm d}/R_{\rm d}$ against $M_{\pm}$. The disk rings appear narrower around more massive stars.

Next, we consider the deciding factors of $\Delta R_{\rm d}/R_{\rm d}$. To simplify the model, we assume that the dust grains are produced from circularly orbiting parent planetesimals. The parent planetesimals experience a gravitational force of $GM_{\pm}$ per unit mass. The created dust receives $GM_{\pm}(1 \quad \beta)$ per unit mass, where β is the ratio of stellar radiation pressure to stellar gravity. For dusts with $\beta < 0.5$, we can estimate the eccentricity e and pericenter $q_{\rm peri}$, as follows:

$$e = \frac{\beta}{1 \quad \beta} \tag{25}$$

$$q_{\rm peri} = R_{\rm pp} \tag{26}$$

(Hahn 2010), where $R_{\rm pp}$ is the orbital radius of the parent planetesimamls. We assume no gravity among the dusts. To calculate $\Delta R_{\rm d}/R_{\rm d}$ as a function of e ($0 < e < 1$) in the $R_{\rm pp}$ normalized system, we distribute 10^7 dust particles following the probability distribution of an orbit with eccentricity e. We randomly set $q_{\rm peri} = 1 \oplus w_{\rm pp}/2$ (i.e., a uniform distribution), where $w_{\rm pp}$ is the normalized width of the location of the parent planetesimals. Assuming a steady-state system, we randomly set the argument of the pericenter within the range $0 < \omega < 2\pi$, and obtain the radial volume density profile of the model for various $w_{\rm pp}$ and e values. We then derive the FWHM and peak location, $\Delta R_{\rm d}$ and $R_{\rm d}$, respectively, of this density profile. The simulated $\Delta R_{\rm d}/R_{\rm d}$s are plotted as functions of e and $w_{\rm pp}$ in Figure 29. We find that

$$\Delta R_{\rm d}/R_{\rm d} \sim w_{\rm pp} \tag{27}$$

for all e. The targets are also plotted on this graph. The eccentricity of each dust particle is calculated by Equation (25), with

$$\beta = 0.574 \frac{L_{\pm}}{L_{\circ}} \frac{M_{\circ}}{M_{\pm}} \frac{1 \text{ g/cm}^3}{\rho_{\rm d}} \frac{1 \ \mu m}{s} \tag{28}$$

(Krivov et al. 2006), where ρ_d is the bulk density of the dusts. Assuming an astronomical silicate composition, we set $s = 1\ \mu m$ and $\rho_d = 3\ g/cm^3$. As $L_\pm \propto M_\pm^{3.4}$, more massive stars have larger β; consequently, their dusts have higher e. Comparing the observed and simulated $\Delta R_d/R_d$, it appears that lower-mass stars have larger w_{pp}, whereas more massive stars have smaller w_{pp} (Figure 29).

The large w_{pp} means that the planetesimals producing the dusts are widely located in the radial direction. We now determine w_{pp} in the planet stirring and self-stirring models. The beginning of the planetesimal collisions at r can be computed by Equation (2) or (3). This radius r is considered as the outer radius of the annulus in which the planetesimals produce the dusts, because both model scenarios propagate the collisional region to the outside. Meanwhile, the inner radius of the belt is the terminal location of the planetesimal collisions. Therefore, w_{pp} can be defined by determining the ending time of the planetesimal collisions. Unfortunately, the collisional ending times have not been predicted in either scenario. Assuming that w_{pp} is smaller for more massive stars, the duration of planetesimals collisions should be shorter for more massive stars. In physical terms, the relative velocities of planetesimals should be high around massive stars, so collisions will be more frequent. Why the parent planetesimal belt is thinner around more massive stars requires additional theoretical analysis.

5.3.3 Collisional timescale

We now estimate the collisional timescale using the derived disk parameters. The collisional timescale is calculated as

$$t_{col} \propto \left(\frac{\tau_r \Omega(r)}{w_{pp}} \right)^{1} \tag{29}$$

(Rodigas et al. 2014), where $\Omega(r) = \sqrt{GM_\pm/r^3}$ is the angular rotation rate at radius r. Assuming that collisions occur at $r = R_d$, we relate the collisional timescale to the stellar age or mass. In this analysis, we use the more reliable width $\Delta R_d/R_d$ instead of the model-dependent width w_{pp}. As $\Delta R_d/R_d \sim w_{pp}$ (Equation (27)), the derived t_{col} should be the upper limit.

Figure 30 plots the upper limit of the collisional timescale against t for each targets. The collisional timescale trends to increase with stellar age. This behavior is easily explained by Equation (29). First, the radial optical depth τ_r decreases with stellar age t (Figure 21), meaning that disks around older stars have reduced volume density. Second, the growth of the disk radius diminishes the angular rotation rate ($\Omega(r) \propto r^{-2/3}$). Consequently, planetesimal collisions become more infrequent as the system ages. Applying this trend to our solar system, the estimated collisional timescale is $t_{col} \lesssim 10$ Myr.

Figure 31 plots the upper limit of the collisional timescale against $M_\pm$ for each target. The collisional timescale trends downward with stellar mass. The radial optical depth τ_r is uncorrelated with $M_\pm$ (Figure 22). Besides increasing the angular rotation rate ($\Omega(r) \propto M_\pm^{1/2}$), more massive stars with narrower widths of parent planetesimals (Section 5.3.2) diminish the collisional timescale.

5.3.4 Scattering asymmetry parameter

As mentioned in Section 4.6.3, high scattering asymmetry ($g > 0.5$) is absent in old systems ($t > 500$ Myr; see Figure 19). This deficiency might be artificially introduced by the small number of old debris disks in our targets. If real, this feature has two plausible causes: 1) disappearance of large-sized grains, and 2) observational bias.

Rayleigh scattering is isotropic, whereas Mie scattering is anisotropic. As Mie scattering occurs when the grain size exceeds the wavelength, the disappearance of large grains diminishes the scattering asymmetry. Older systems could lose large grains by repetitive grain-grain collisions. However, dust size is difficult to be quantified by g alone, and this phenomenon needs verification in multi-band observations.

The optical depths reduce as the system ages (Figure 22). To be detected, the grains in old debris disks need to scatter the starlight efficiently to observers. In high-g disks around old stars, most of the photons are forward-scattered in various directions rather than being directed toward the observer. This observational bias needs validation in spatially-resolved targets.

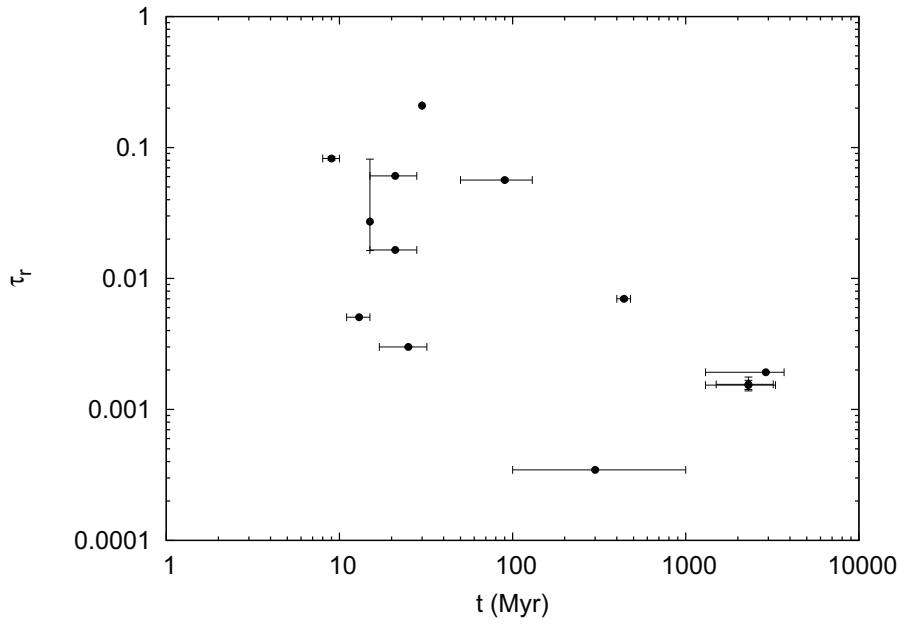

Figure 21: Radial optical depth versus stellar age.

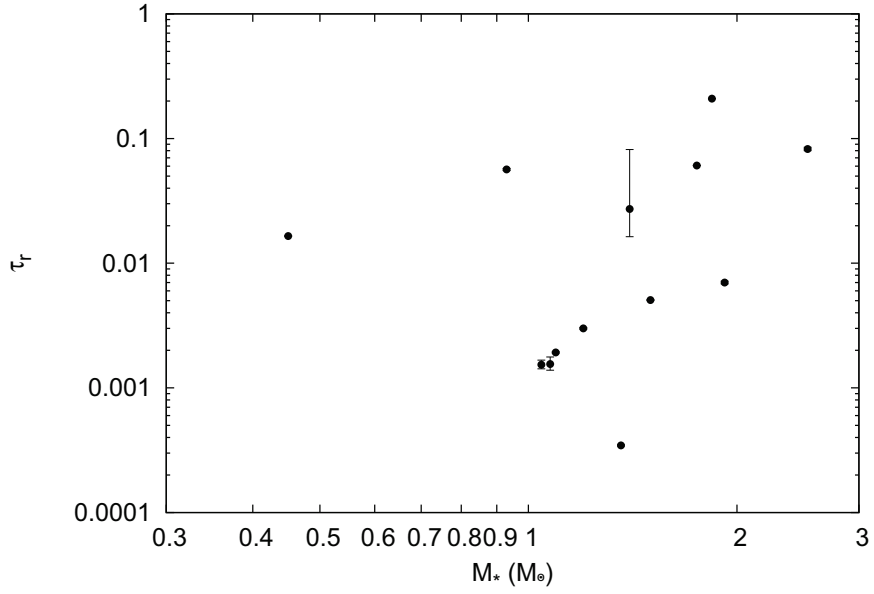

Figure 22: Radial optical depth versus stellar mass.

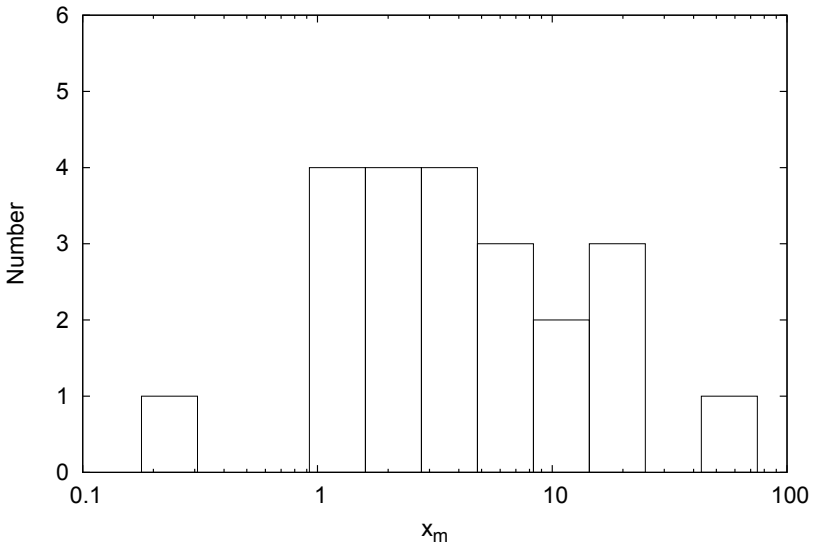

Figure 23: Histogram showing the distribution of x_m in the self-stirring scenario. The six targets with $x_m \sim 10$ cannot maintain disk gravitational stability in the protoplanetary stage.

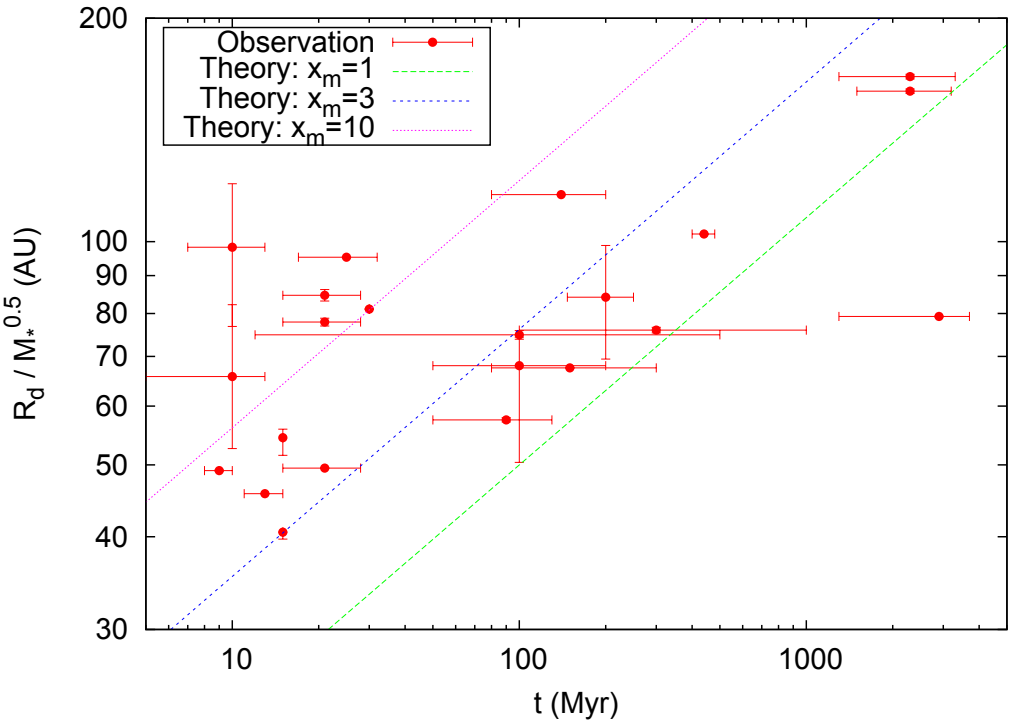

Figure 24: Disk radii (calibrated by stellar mass) versus stellar age in the self-stirring scenario. The green, blue, and magenta lines indicate the disk radii in the self-stirring model with x_m = 1, 3, and 10, respectively. Half of the young targets (t < 30 Myr) lie above the x_m = 10 line, which marks the upper limit of disk gravitational stability in the protoplanetary stage.

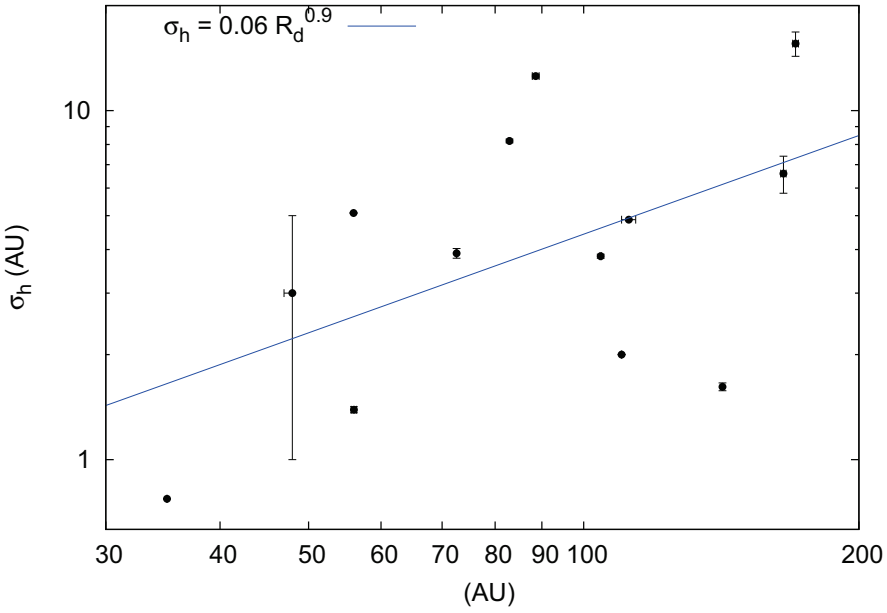

Figure 25: $R_{\rm d}$ versus σ_h. The blue line is the best-fit line. σ_h appears to be proportional to $R_{\rm d}$.

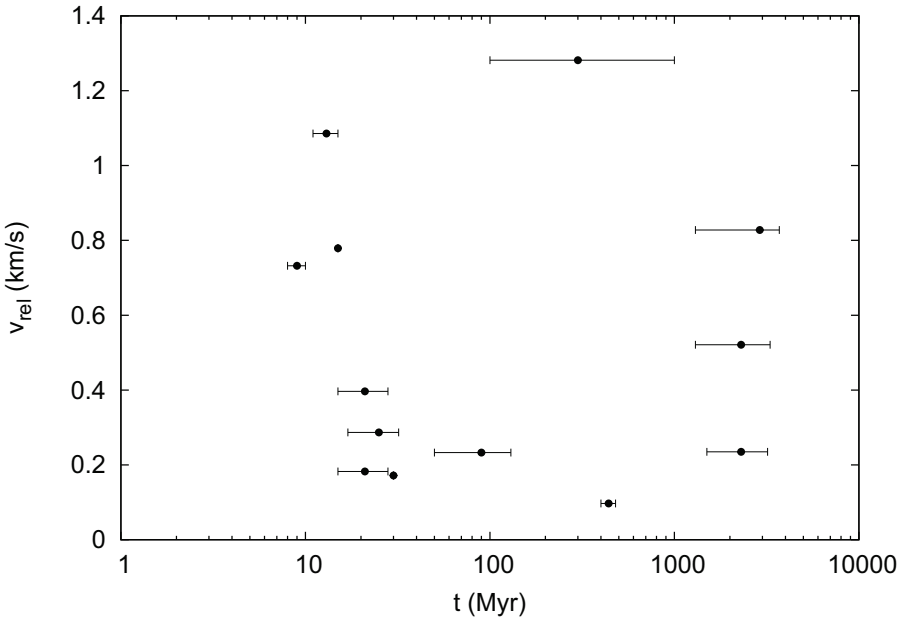

Figure 26: Velocity dispersion versus stellar age.

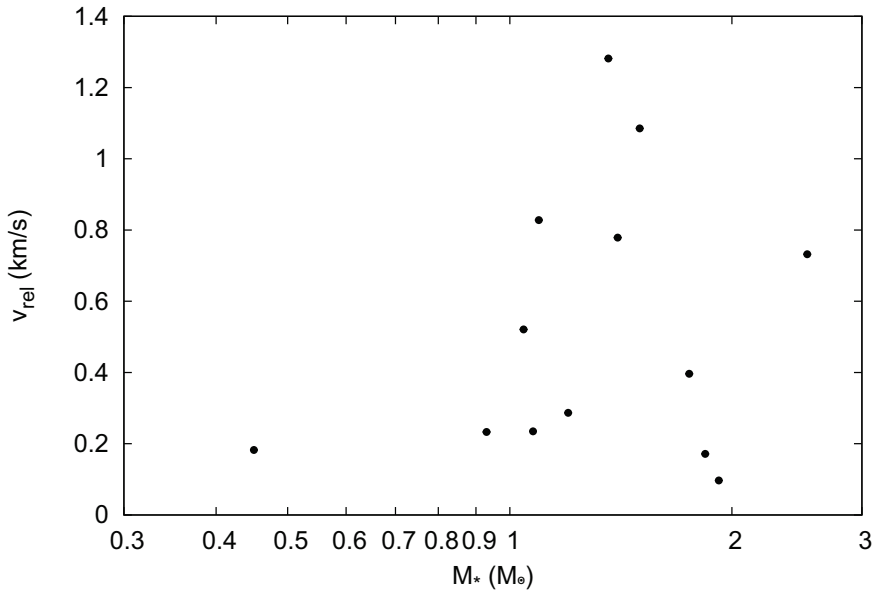

Figure 27: Velocity dispersion versus stellar mass.

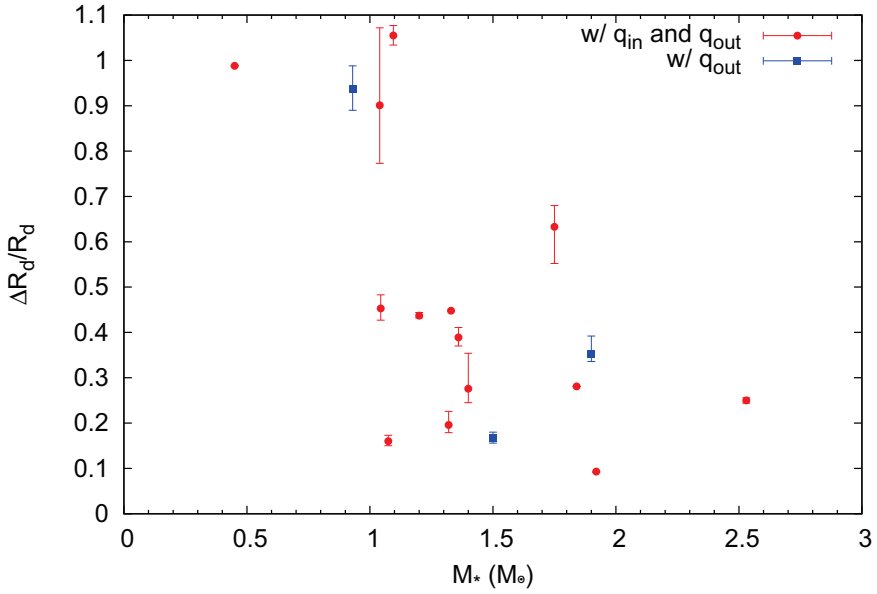

Figure 28: Normalized ring width versus stellar mass. The red circles and blue squares represent $\Delta R_{\rm d}/R_{\rm d}$ derived from $q_{\rm in}$ and $q_{\rm out}$ (Equation (21)) and from $q_{\rm out}$ only (Equation (23)), respectively. $\Delta R_{\rm d}/R_{\rm d}$ appears to decrease with increasing $M_{\pm}$.

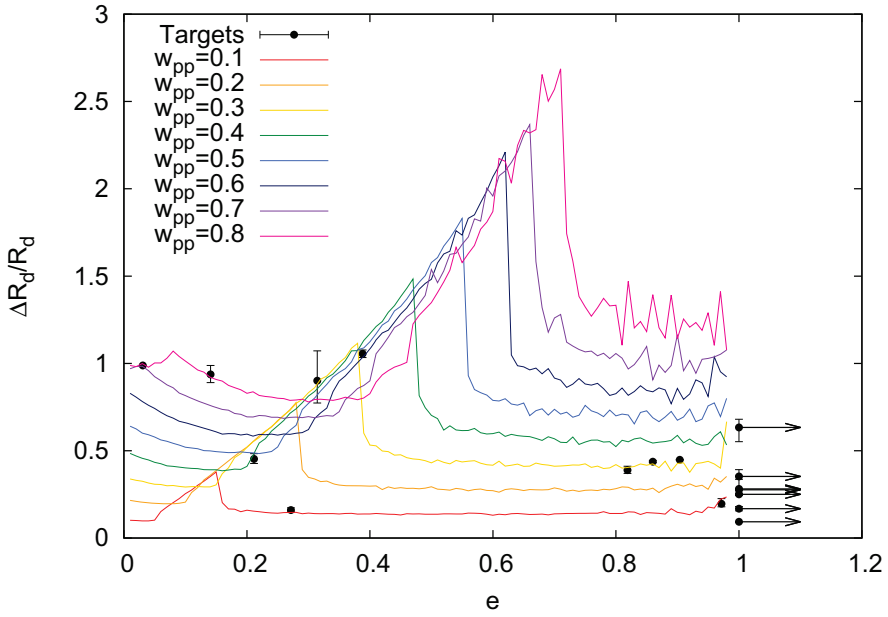

Figure 29: Simulated $\Delta R_{\rm d}/R_{\rm d}$ as functions of dust eccentricity. The different colors represent different initial values of $w_{\rm pp}$. The black circles represent the normalized ring widths of the targets. The eccentricities are calculated by Equations (25) and (28). The targets with smaller grain eccentricities ($e < 0.4$) appear to have wider parent planetesimals belts ($w_{\rm pp} \gtrsim 0.4$). Conversely, the targets with the larger grain eccentricities ($e > 0.8$) appear to have the thinner parent planetesimals belts ($w_{\rm pp} \lesssim 0.3$).

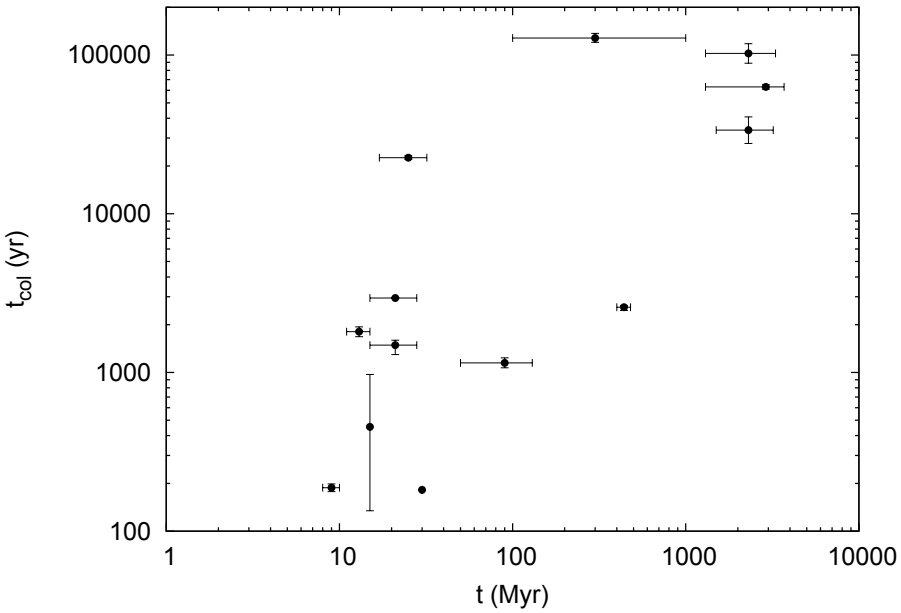

Figure 30: Upper limit of the collisional timescale versus stellar age. Planetesimal collisions appear to be less frequent in older targets.

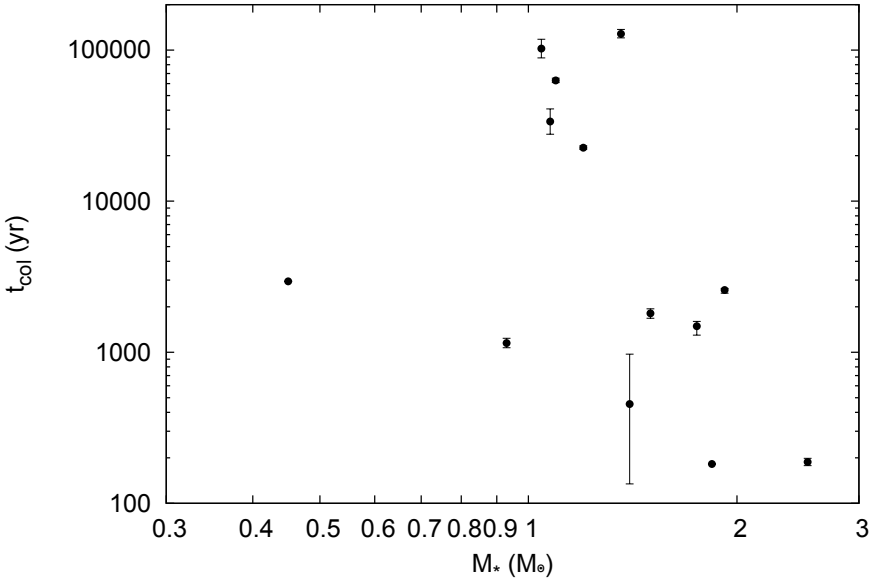

Figure 31: Upper limit of collisional timescale versus the stellar mass. Planetesimal collisions appear to be more frequent in system with more massive stars.

6 Summary

We investigated the morphologies of 22 debris disks. Nine of the disk morphologies were derived by model fitting; the remainder were cited from previous studies. The main results are summarized as follows:

1. The disk radii appear to increase with stellar age. The relation is $R_{\rm d} \propto t^{0.1\ 0.2}$, with a correlation coefficient of 0.57 on a log-log plot. This trend is consistent with the planetary stirring and self-stirring scenarios.

2. The disk radii also apparently increase with stellar mass. The relation is $R_{\rm d} \propto M_{\pm}^{0.2\ 0.7}$, with a correlation coefficient of 0.51 on a log-log plot. This trend is consistent with the self-stirring scenario.

3. We examine the possible mechanism of planetary stirring in three debris disks containing detected planets (beta Pic, HD 10647, HD 106906). The planetary stirring model can explain only the presence of the inner disk of beta Pic (at radius $\propto$ 60 AU) by a $\propto 10 M_J$ planet ($\propto$ 9 AU).

4. The vertical thickness is approximately proportional to the disk radius. The velocity dispersions is nearly independent of stellar age and mass.

5. The ring widths appear to decrease with stellar mass. The collisional duration might be shorter for the more massive star.

6. The scattering asymmetry parameter g might reach an upper limit in old stars. This can be explained by the disappearance of large grains or by observational bias.

References

M. Ahmic, B. Croll, and P. Artymowicz. Dust Distribution in the β Pictoris Circumstellar Disks. ApJ, 705:529–542, November 2009.

C. Allende Prieto and D. L. Lambert. Fundamental parameters of nearby stars from the comparison with evolutionary calculations: masses, radii and effective temperatures. A&A, 352:555–562, December 1999.

D. Apai, G. Schneider, C. A. Grady, M. C. Wyatt, A.-M. Lagrange, M. J. Kuchner, C. J. Stark, and S. H. Lubow. The Inner Disk Structure, Disk-Planet Interactions, and Temporal Evolution in the β Pictoris System: A Two-epoch HST/STIS Coronagraphic Study. ApJ, 800:136, February 2015.

D. R. Ardila, D. A. Golimowski, J. E. Krist, M. Clampin, J. P. Williams, J. P. Blakeslee, H. C. Ford, G. F. Hartig, and G. D. Illingworth. A Resolved Debris Disk around the G2 V Star HD 107146. ApJL, 617:L147–L150, December 2004.

J.-C. Augereau and H. Beust. On the AU Microscopii debris disk. Density profiles, grain properties, and dust dynamics. A&A, 455:987–999, September 2006.

J. C. Augereau, A. M. Lagrange, D. Mouillet, J. C. B. Papaloizou, and P. A. Grorod. On the HR 4796 A circumstellar disk. A&A, 348:557–569, August 1999.

H. H. Aumann, C. A. Beichman, F. C. Gillett, T. de Jong, J. R. Houck, F. J. Low, G. Neugebauer, R. G. Walker, and P. R. Wesselius. Discovery of a shell around Alpha Lyrae. ApJL, 278:L23–L27, March 1984.

V. Bailey, T. Meshkat, M. Reiter, K. Morzinski, J. Males, K. Y. L. Su, P. M. Hinz, M. Kenworthy, D. Stark, E. Mamajek, R. Briguglio, L. M. Close, K. B. Follette, A. Puglisi, T. Rodigas, A. J. Weinberger, and M. Xompero. HD 106906 b: A Planetary-mass Companion Outside a Massive Debris Disk. ApJL, 780:L4, January 2014.

I. Baraffe, G. Chabrier, F. Allard, and P. H. Hauschildt. Evolutionary models for solar metallicity low-mass stars: mass-magnitude relationships and color-magnitude diagrams. A&A, 337:403–412, September 1998.

G. Bertelli, L. Girardi, P. Marigo, and E. Nasi. Scaled solar tracks and isochrones in a large region of the Z-Y plane. I. From the ZAMS to the TP-AGB end for 0.15-2.5 $M_{\circ}$ stars. A&A, 484: 815–830, June 2008.

A. S. Binks and R. D. Jeffries. A lithium depletion boundary age of 21 Myr for the Beta Pictoris moving group. MNRAS, 438:L11–L15, February 2014.

A. Boccaletti, J.-C. Augereau, A.-M. Lagrange, J. Milli, P. Baudoz, D. Mawet, D. Mouillet, J. Lebreton, and A.-L. Maire. Morphology of the very inclined debris disk around HD 32297. A&A, 544:A85, August 2012.

E. Buenzli, C. Thalmann, A. Vigan, A. Boccaletti, G. Chauvin, J. C. Augereau, M. R. Meyer, F. Ménard, S. Desidera, S. Messina, T. Henning, J. Carson, G. Montagnier, J. L. Beuzit, M. Bonavita, A. Eggenberger, A. M. Lagrange, D. Mesa, D. Mouillet, and S. P. Quanz. Dissecting the Moth: discovery of an off-centered ring in the HD 61005 debris disk with high-resolution imaging. A&A, 524:L1, December 2010.

R. P. Butler, J. T. Wright, G. W. Marcy, D. A. Fischer, S. S. Vogt, C. G. Tinney, H. R. A. Jones, B. D. Carter, J. A. Johnson, C. McCarthy, and A. J. Penny. Catalog of Nearby Exoplanets. ApJ, 646:505–522, July 2006.

L. Casagrande, R. Schönrich, M. Asplund, S. Cassisi, I. Ramírez, J. Meléndez, T. Bensby, and S. Feltzing. New constraints on the chemical evolution of the solar neighbourhood and Galactic disc(s). Improved astrophysical parameters for the Geneva-Copenhagen Survey. A&A, 530: A138, June 2011.

C. H. Chen, T. Mittal, M. Kuchner, W. J. Forrest, C. M. Lisse, P. Manoj, B. A. Sargent, and D. M. Watson. The Spitzer Infrared Spectrograph Debris Disk Catalog. I. Continuum Analysis of Unresolved Targets. ApJS, 211:25, April 2014.

E. Chiang, E. Kite, P. Kalas, J. R. Graham, and M. Clampin. Fomalhaut's Debris Disk and Planet: Constraining the Mass of Fomalhaut b from disk Morphology. ApJ, 693:734–749, March 2009.

É. Choquet, M. D. Perrin, C. H. Chen, R. Soummer, L. Pueyo, J. B. Hagan, E. Gofas-Salas, A. Rajan, D. A. Golimowski, D. C. Hines, G. Schneider, J. Mazoyer, J.-C. Augereau, J. Debes, C. C. Stark, S. Wolff, M. N'Diaye, and K. Hsiao. First images of debris disks around TWA 7, TWA 25, HD 35650, and HD 377. *ArXiv e-prints*, December 2015.

T. Currie, J. Debes, T. J. Rodigas, A. Burrows, Y. Itoh, M. Fukagawa, S. J. Kenyon, M. Kuchner, and S. Matsumura. Direct Imaging Confirmation and Characterization of a Dust-enshrouded Candidate Exoplanet Orbiting Fomalhaut. ApJL, 760:L32, December 2012a.

T. Currie, T. J. Rodigas, J. Debes, P. Plavchan, M. Kuchner, H. Jang-Condell, D. Wilner, S. Andrews, A. Kraus, S. Dahm, and T. Robitaille. Keck/NIRC2 Imaging of the Warped, Asymmetric Debris Disk around HD 32297. ApJ, 757:28, September 2012b.

T. Currie, C. M. Lisse, M. Kuchner, N. Madhusudhan, S. J. Kenyon, C. Thalmann, J. Carson, and J. Debes. Direct Imaging and Spectroscopy of a Young Extrasolar Kuiper Belt in the Nearest OB Association. ApJL, 807:L7, July 2015.

R. J. De Rosa, J. Patience, P. A. Wilson, A. Schneider, S. J. Wiktorowicz, A. Vigan, C. Marois, I. Song, B. Macintosh, J. R. Graham, R. Doyon, M. S. Bessell, S. Thomas, and O. Lai. The VAST Survey - III. The multiplicity of A-type stars within 75 pc. MNRAS, 437:1216–1240, January 2014.

S. F. Dermott, T. J. J. Kehoe, D. D. Durda, K. Grogan, and D. Nesvorný. Recent rubble-pile origin of asteroidal solar system dust bands and asteroidal interplanetary dust particles. In B. Warmbein, editor, *Asteroids, Comets, and Meteors: ACM 2002*, volume 500 of *ESA Special Publication*, pages 319–322, November 2002.

J. K. Donaldson, J. Lebreton, A. Roberge, J.-C. Augereau, and A. V. Krivov. Modeling the HD 32297 Debris Disk with Far-infrared Herschel Data. ApJ, 772:17, July 2013.

C. Eiroa, J. P. Marshall, A. Mora, B. Montesinos, O. Absil, J. C. Augereau, A. Bayo, G. Bryden, W. Danchi, C. del Burgo, S. Ertel, M. Fridlund, A. M. Heras, A. V. Krivov, R. Launhardt, R. Liseau, T. Löhne, J. Maldonado, G. L. Pilbratt, A. Roberge, J. Rodmann, J. Sanz-Forcada, E. Solano, K. Stapelfeldt, P. Thébault, S. Wolf, D. Ardila, M. Arévalo, C. Beichmann, V. Faramaz, B. M. González-García, R. Gutiérrez, J. Lebreton, R. Martínez-Arnáiz, G. Meeus, D. Montes, G. Olofsson, K. Y. L. Su, G. J. White, D. Barrado, M. Fukagawa, E. Grün, I. Kamp, R. Lorente, A. Morbidelli, S. Müller, H. Mutschke, T. Nakagawa, I. Ribas, and H. Walker. DUst around NEarby Stars. The survey observational results. A&A, 555:A11, July 2013.

M. P. Fitzgerald, P. G. Kalas, G. Duchêne, C. Pinte, and J. R. Graham. The AU Microscopii Debris Disk: Multiwavelength Imaging and Modeling. ApJ, 670:536–556, November 2007.

E. Gaidos, A. W. Mann, S. Lépine, A. Buccino, D. James, M. Ansdell, R. Petrucci, P. Mauas, and E. J. Hilton. Trumpeting M dwarfs with CONCH-SHELL: a catalogue of nearby cool host-stars for habitable exoplanets and life. MNRAS, 443:2561–2578, September 2014.

R. Galicher, C. Marois, B. Zuckerman, and B. Macintosh. Fomalhaut b: Independent Analysis of the Hubble Space Telescope Public Archive Data. ApJ, 769:42, May 2013.

D. A. Golimowski, J. E. Krist, K. R. Stapelfeldt, C. H. Chen, D. R. Ardila, G. Bryden, M. Clampin, H. C. Ford, G. D. Illingworth, P. Plavchan, G. H. Rieke, and K. Y. L. Su. Hubble and Spitzer Space Telescope Observations of the Debris Disk around the nearby K Dwarf HD 92945. AJ, 142:30, July 2011.

D. B. Guenther, P. Demarque, Y.-C. Kim, and M. H. Pinsonneault. Standard solar model. ApJ, 387:372–393, March 1992.

J. M. Hahn. Diagnosing Circumstellar Debris Disks. ApJ, 719:1699–1714, August 2010.

S. R. Heap, D. J. Lindler, T. M. Lanz, R. H. Cornett, I. Hubeny, S. P. Maran, and B. Woodgate. Space Telescope Imaging Spectrograph Coronagraphic Observations of β Pictoris. ApJ, 539: 435–444, August 2000.

L.-W. Hung, G. Duchêne, P. Arriaga, M. P. Fitzgerald, J. Maire, C. Marois, M. A. Millar-Blanchaer, S. Bruzzone, A. Rajan, L. Pueyo, P. G. Kalas, R. J. De Rosa, J. R. Graham, Q. Konopacky, S. G. Wolff, S. M. Ammons, C. H. Chen, J. K. Chilcote, Z. H. Draper, T. M. Esposito, B. Gerard, S. Goodsell, A. Greenbaum, P. Hibon, S. Hinkley, B. Macintosh, F. Marchis, S. Metchev, E. L. Nielsen, R. Oppenheimer, J. L. Patience, M. D. Perrin, F. T. Rantakyrö, A. Sivaramakrishnan, J. J. Wang, K. Ward-Duong, and S. J. Wiktorowicz. First Scattered-light Image of the Debris Disk around HD 131835 with the Gemini Planet Imager. ApJL, 815:L14, December 2015.

P. Kalas, J. R. Graham, E. Chiang, M. P. Fitzgerald, M. Clampin, E. S. Kite, K. Stapelfeldt, C. Marois, and J. Krist. Optical Images of an Exosolar Planet 25 Light-Years from Earth. *Science*, 322:1345, November 2008.

P. Kalas, J. R. Graham, M. P. Fitzgerald, and M. Clampin. STIS Coronagraphic Imaging of Fomalhaut: Main Belt Structure and the Orbit of Fomalhaut b. ApJ, 775:56, September 2013.

P. G. Kalas, A. Rajan, J. J. Wang, M. A. Millar-Blanchaer, G. Duchene, C. Chen, M. P. Fitzgerald, R. Dong, J. R. Graham, J. Patience, B. Macintosh, R. Murray-Clay, B. Matthews, J. Rameau, C. Marois, J. Chilcote, R. J. De Rosa, R. Doyon, Z. H. Draper, S. Lawler, S. M. Ammons, P. Arriaga, J. Bulger, T. Cotten, K. B. Follette, S. Goodsell, A. Greenbaum, P. Hibon, S. Hinkley, L.-W. Hung, P. Ingraham, Q. Konapacky, D. Lafreniere, J. E. Larkin, D. Long, J. Maire, F. Marchis, S. Metchev, K. M. Morzinski, E. L. Nielsen, R. Oppenheimer, M. D. Perrin, L. Pueyo, F. T. Rantakyrö, J.-B. Ruffio, L. Saddlemyer, D. Savransky, A. C. Schneider, A. Sivaramakrishnan, R. Soummer, I. Song, S. Thomas, G. Vasisht, K. Ward-Duong, S. J. Wiktorowicz, and S. G. Wolff. Direct Imaging of an Asymmetric Debris Disk in the HD 106906 Planetary System. ApJ, 814:32, November 2015.

S. J. Kenyon and B. C. Bromley. Collisional Cascades in Planetesimal Disks. I. Stellar Flybys. AJ, 123:1757–1775, March 2002.

S. J. Kenyon and B. C. Bromley. Variations on Debris Disks: Icy Planet Formation at 30-150 AU for 1-3 M_{solar} Main-Sequence Stars. ApJS, 179:451–483, December 2008.

J. E. Krist, D. R. Ardila, D. A. Golimowski, M. Clampin, H. C. Ford, G. D. Illingworth, G. F. Hartig, F. Bartko, N. Benítez, J. P. Blakeslee, R. J. Bouwens, L. D. Bradley, T. J. Broadhurst,

R. A. Brown, C. J. Burrows, E. S. Cheng, N. J. G. Cross, R. Demarco, P. D. Feldman, M. Franx, T. Goto, C. Gronwall, B. Holden, N. Homeier, L. Infante, R. A. Kimble, M. P. Lesser, A. R. Martel, S. Mei, F. Menanteau, G. R. Meurer, G. K. Miley, V. Motta, M. Postman, P. Rosati, M. Sirianni, W. B. Sparks, H. D. Tran, Z. I. Tsvetanov, R. L. White, and W. Zheng. Hubble Space Telescope Advanced Camera for Surveys Coronagraphic Imaging of the AU Microscopii Debris Disk. AJ, 129:1008–1017, February 2005.

J. E. Krist, K. R. Stapelfeldt, G. Bryden, G. H. Rieke, K. Y. L. Su, C. C. Chen, C. A. Beichman, D. C. Hines, L. M. Rebull, A. Tanner, D. E. Trilling, M. Clampin, and A. Gáspár. HST and Spitzer Observations of the HD 207129 Debris Ring. AJ, 140:1051–1061, October 2010.

J. E. Krist, K. R. Stapelfeldt, G. Bryden, and P. Plavchan. Hubble Space Telescope Observations of the HD 202628 Debris Disk. AJ, 144:45, August 2012.

A. V. Krivov, T. Löhne, and M. Sremčević. Dust distributions in debris disks: effects of gravity, radiation pressure and collisions. A&A, 455:509–519, August 2006.

D. Lafrenière, C. Marois, R. Doyon, D. Nadeau, and É. Artigau. A New Algorithm for Point-Spread Function Subtraction in High-Contrast Imaging: A Demonstration with Angular Differential Imaging. ApJ, 660:770–780, May 2007.

A.-M. Lagrange, D. Gratadour, G. Chauvin, T. Fusco, D. Ehrenreich, D. Mouillet, G. Rousset, D. Rouan, F. Allard, É. Gendron, J. Charton, L. Mugnier, P. Rabou, J. Montri, and F. Lacombe. A probable giant planet imaged in the β Pictoris disk. VLT/NaCo deep L'-band imaging. A&A, 493:L21–L25, January 2009.

A.-M. Lagrange, M. Bonnefoy, G. Chauvin, D. Apai, D. Ehrenreich, A. Boccaletti, D. Gratadour, D. Rouan, D. Mouillet, S. Lacour, and M. Kasper. A Giant Planet Imaged in the Disk of the Young Star β Pictoris. *Science*, 329:57, July 2010.

A.-M. Lagrange, M. Langlois, R. Gratton, A.-L. Maire, J. Milli, J. Olofsson, A. Vigan, V. Bailey, D. Mesa, G. Chauvin, A. Boccaletti, R. Galicher, J. M. Girard, M. Bonnefoy, M. Samland, F. Menard, T. Henning, M. Kenworthy, C. Thalmann, H. Beust, J.-L. Beuzit, W. Brandner, E. Buenzli, A. Cheetham, M. Janson, H. le Coroller, J. Lannier, D. Mouillet, S. Peretti, C. Perrot, G. Salter, E. Sissa, Z. Wahhaj, L. Abe, S. Desidera, M. Feldt, F. Madec, D. Perret, C. Petit, P. Rabou, C. Soenke, and L. Weber. A narrow, edge-on disk resolved around HD 106906 with SPHERE. *ArXiv e-prints*, October 2015.

C. F. Manara, L. Testi, E. Rigliaco, J. M. Alcalá, A. Natta, B. Stelzer, K. Biazzo, E. Covino, S. Covino, G. Cupani, V. D'Elia, and S. Randich. X-shooter spectroscopy of young stellar objects. II. Impact of chromospheric emission on accretion rate estimates. A&A, 551:A107, March 2013.

A. W. Mann, E. Gaidos, and M. Ansdell. Spectro-thermometry of M Dwarfs and Their Candidate Planets: Too Hot, Too Cool, or Just Right? ApJ, 779:188, December 2013.

C. Marois, D. Lafrenière, R. Doyon, B. Macintosh, and D. Nadeau. Angular Differential Imaging: A Powerful High-Contrast Imaging Technique. ApJ, 641:556–564, April 2006.

J. P. Marshall, T. Löhne, B. Montesinos, A. V. Krivov, C. Eiroa, O. Absil, G. Bryden, J. Maldonado, A. Mora, J. Sanz-Forcada, D. Ardila, J.-C. Augereau, A. Bayo, C. Del Burgo, W. Danchi, S. Ertel, D. Fedele, M. Fridlund, J. Lebreton, B. M. González-García, R. Liseau, G. Meeus, S. Müller, G. L. Pilbratt, A. Roberge, K. Stapelfeldt, P. Thébault, G. J. White, and S. Wolf. A Herschel resolved far-infrared dust ring around HD 207129. A&A, 529:A117, May 2011.

B. C. Matthews, A. V. Krivov, M. C. Wyatt, G. Bryden, and C. Eiroa. Observations, Modeling, and Theory of Debris Disks. *Protostars and Planets VI*, pages 521–544, 2014.

J. Mazoyer, A. Boccaletti, J.-C. Augereau, A.-M. Lagrange, R. Galicher, and P. Baudoz. Is the HD 15115 inner disk really asymmetrical? A&A, 569:A29, September 2014.

M. A. Millar-Blanchaer, J. R. Graham, L. Pueyo, P. Kalas, R. I. Dawson, J. Wang, M. D. Perrin, D.-S. moon, B. Macintosh, S. M. Ammons, T. Barman, A. Cardwell, C. H. Chen, E. Chiang, J. Chilcote, T. Cotten, R. J. De Rosa, Z. H. Draper, J. Dunn, G. Duchêne, T. M. Esposito, M. P. Fitzgerald, K. B. Follette, S. J. Goodsell, A. Z. Greenbaum, M. Hartung, P. Hibon, S. Hinkley, P. Ingraham, R. Jensen-Clem, Q. Konopacky, J. E. Larkin, D. Long, J. Maire, F. Marchis, M. S. Marley, C. Marois, K. M. Morzinski, E. L. Nielsen, D. W. Palmer, R. Oppenheimer, L. Poyneer, A. Rajan, F. T. Rantakyrö, J.-B. Ruffio, N. Sadakuni, L. Saddlemyer, A. C. Schneider, A. Sivaramakrishnan, R. Soummer, S. Thomas, G. Vasisht, D. Vega, J. K. Wallace, K. Ward-Duong, S. J. Wiktorowicz, and S. G. Wolff. Beta Pictoris' Inner Disk in Polarized Light and New Orbital Parameters for Beta Pictoris b. ApJ, 811:18, September 2015.

J. Milli, D. Mouillet, A.-M. Lagrange, A. Boccaletti, D. Mawet, G. Chauvin, and M. Bonnefoy. Impact of angular differential imaging on circumstellar disk images. A&A, 545:A111, September 2012.

A. Moór, P. Ábrahám, A. Juhász, C. Kiss, I. Pascucci, Á. Kóspál, D. Apai, T. Henning, T. Csengeri, and C. Grady. Molecular Gas in Young Debris Disks. ApJL, 740:L7, October 2011a.

A. Moór, I. Pascucci, Á. Kóspál, P. Ábrahám, T. Csengeri, L. L. Kiss, D. Apai, C. Grady, T. Henning, C. Kiss, D. Bayliss, A. Juhász, J. Kovács, and T. Szalai. Structure and Evolution of Debris Disks Around F-type Stars. I. Observations, Database, and Basic Evolutionary Aspects. ApJS, 193:4, March 2011b.

A. Moór, Á. Kóspál, P. Ábrahám, D. Apai, Z. Balog, C. Grady, T. Henning, A. Juhász, C. Kiss, A. V. Krivov, N. Pawellek, and G. M. Szabó. Stirring in massive, young debris discs from spatially resolved Herschel images. MNRAS, 447:577–597, February 2015.

A. Moro-Martin. *Dusty Planetary Systems*, page 431. 2013.

A. J. Mustill and M. C. Wyatt. Debris disc stirring by secular perturbations from giant planets. MNRAS, 399:1403–1414, November 2009.

J. Najita and J. P. Williams. An 850 μm Survey for Dust around Solar-Mass Stars. ApJ, 635: 625–635, December 2005.

A. C. Quillen, A. Morbidelli, and A. Moore. Planetary embryos and planetesimals residing in thin debris discs. MNRAS, 380:1642–1648, October 2007.

J. H. Rhee, I. Song, B. Zuckerman, and M. McElwain. Characterization of Dusty Debris Disks: The IRAS and Hipparcos Catalogs. ApJ, 660:1556–1571, May 2007.

T. J. Rodigas, P. M. Hinz, J. Leisenring, V. Vaitheeswaran, A. J. Skemer, M. Skrutskie, K. Y. L. Su, V. Bailey, G. Schneider, L. Close, F. Mannucci, S. Esposito, C. Arcidiacono, E. Pinna, J. Argomedo, G. Agapito, D. Apai, G. Bono, K. Boutsia, R. Briguglio, G. Brusa, L. Busoni, G. Cresci, T. Currie, S. Desidera, J. Eisner, R. Falomo, L. Fini, K. Follette, A. Fontana, P. Garnavich, R. Gratton, R. Green, J. C. Guerra, J. M. Hill, W. F. Hoffmann, T. J. Jones, M. Krejny, C. Kulesa, J. Males, E. Masciadri, D. Mesa, D. McCarthy, M. Meyer, D. Miller, M. J. Nelson, A. Puglisi, F. Quiros-Pacheco, A. Riccardi, E. Sani, P. Stefanini, V. Testa, J. Wilson, C. E. Woodward, and M. Xompero. The Gray Needle: Large Grains in the HD 15115 Debris Disk from LBT/PISCES/Ks and LBTI/LMIRcam/L' Adaptive Optics Imaging. ApJ, 752:57, June 2012.

T. J. Rodigas, R. Malhotra, and P. M. Hinz. Predictions for Shepherding Planets in Scattered Light Images of Debris Disks. ApJ, 780:65, January 2014.

T. J. Rodigas, C. C. Stark, A. Weinberger, J. H. Debes, P. M. Hinz, L. Close, C. Chen, P. S. Smith, J. R. Males, A. J. Skemer, A. Puglisi, K. B. Follette, K. Morzinski, Y.-L. Wu, R. Briguglio, S. Esposito, E. Pinna, A. Riccardi, G. Schneider, and M. Xompero. On the Morphology and Chemical Composition of the HR 4796A Debris Disk. ApJ, 798:96, January 2015.

G. Schneider, C. A. Grady, D. C. Hines, C. C. Stark, J. H. Debes, J. Carson, M. J. Kuchner, M. D. Perrin, A. J. Weinberger, J. P. Wisniewski, M. D. Silverstone, H. Jang-Condell, T. Henning, B. E. Woodgate, E. Serabyn, A. Moro-Martin, M. Tamura, P. M. Hinz, and T. J. Rodigas. Probing for Exoplanets Hiding in Dusty Debris Disks: Disk Imaging, Characterization, and Exploration with HST/STIS Multi-roll Coronagraphy. AJ, 148:59, October 2014.

E. J. Shaya and R. P. Olling. Very Wide Binaries and Other Comoving Stellar Companions: A Bayesian Analysis of the Hipparcos Catalogue. ApJS, 192:2, January 2011.

B. A. Smith and R. J. Terrile. A circumstellar disk around Beta Pictoris. *Science*, 226:1421–1424, December 1984.

I. A. G. Snellen, B. R. Brandl, R. J. de Kok, M. Brogi, J. Birkby, and H. Schwarz. Fast spin of the young extrasolar planet β Pictoris b. Nature, 509:63–65, May 2014.

R. Soummer, L. Pueyo, and J. Larkin. Detection and Characterization of Exoplanets and Disks Using Projections on Karhunen-Loève Eigenimages. ApJL, 755:L28, August 2012.

R. Soummer, M. D. Perrin, L. Pueyo, É. Choquet, C. Chen, D. A. Golimowski, J. Brendan Hagan, T. Mittal, M. Moerchen, M. N'Diaye, A. Rajan, S. Wolff, J. Debes, D. C. Hines, and G. Schneider. Five Debris Disks Newly Revealed in Scattered Light from the Hubble Space Telescope NICMOS Archive. ApJL, 786:L23, May 2014.

K. Stapelfeldt, J. Krist, G. Bryden, and C. Chen. An HST/Spitzer Study of the HD 10647 Debris Disk. In *In the Spirit of Bernard Lyot: The Direct Detection of Planets and Circumstellar Disks in the 21st Century*, June 2007.

C. C. Stark, G. Schneider, A. J. Weinberger, J. H. Debes, C. A. Grady, H. Jang-Condell, and M. J. Kuchner. Revealing Asymmetries in the HD 181327 Debris Disk: A Recent Massive Collision or Interstellar Medium Warping. ApJ, 789:58, July 2014.

G. Takeda, E. B. Ford, A. Sills, F. A. Rasio, D. A. Fischer, and J. A. Valenti. Structure and Evolution of Nearby Stars with Planets. II. Physical Properties of ˜1000 Cool Stars from the SPOCS Catalog. ApJS, 168:297–318, February 2007.

J. A. Valenti and D. A. Fischer. Spectroscopic Properties of Cool Stars (SPOCS). I. 1040 F, G, and K Dwarfs from Keck, Lick, and AAT Planet Search Programs. ApJS, 159:141–166, July 2005.

C. Vitense, A. V. Krivov, H. Kobayashi, and T. Löhne. An improved model of the Edgeworth-Kuiper debris disk. A&A, 540:A30, April 2012.

Z. Wahhaj, M. C. Liu, E. L. Nielsen, B. A. Biller, T. L. Hayward, L. M. Close, J. R. Males, A. Skemer, C. Ftaclas, M. Chun, N. Thatte, M. Tecza, E. L. Shkolnik, M. Kuchner, I. N. Reid, E. M. de Gouveia Dal Pino, S. H. P. Alencar, J. Gregorio-Hetem, A. Boss, D. N. C. Lin, and D. W. Toomey. The Gemini Planet-finding Campaign: The Frequency Of Giant Planets around Debris Disk Stars. ApJ, 773:179, August 2013.

Z. Wahhaj, M. C. Liu, B. A. Biller, E. L. Nielsen, T. L. Hayward, M. Kuchner, L. M. Close, M. Chun, C. Ftaclas, and D. W. Toomey. The Gemini NICI planet-finding campaign: The offset ring of HR 4796 A. A&A, 567:A34, July 2014.

M. C. Wyatt. Evolution of Debris Disks. ARA&A, 46:339–383, September 2008.

F. Xia and Y.-N. Fu. The V-band Empirical Mass-luminosity Relation for Main Sequence Stars. ChA&A, 34:277–287, July 2010.

B. Zuckerman and I. Song. Dusty Debris Disks as Signposts of Planets: Implications for Spitzer Space Telescope. ApJ, 603:738–743, March 2004.

B. Zuckerman and I. Song. A 40 Myr Old Gaseous Circumstellar Disk at 49 Ceti: Massive CO-rich Comet Clouds at Young A-type Stars. ApJ, 758:77, October 2012.

A PCA

This Appendix describes the PCA reduction for making reference images. Next, we mention the difference between PCA and LOCI.

A.1 Procedure

PCA reduction proceeds through the following three steps.

1. Matrix construction

2. Singular value decomposition

3. Linear combination of bases

We first construct the matrix for singular value decomposition. The reference image is built from N images and the pixel number is $x_n * y_m$. These N images exclude the science image which is to be subtracted. The pixel values are arrayed as

$$\mathbf{A} = \begin{pmatrix} I_1(1,1) & \dots & I_1(x,y) & \dots & I_1(x_n,y_m) \\ I_2(1,1) & \dots & I_2(x,y) & \dots & I_2(x_n,y_m) \\ \vdots & & \vdots & & \vdots \\ I_i(1,1) & \dots & I_i(x,y) & \dots & I_i(x_n,y_m) \\ \vdots & & \vdots & & \vdots \\ I_N(1,1) & \dots & I_N(x,y) & \dots & I_N(x_n,y_m) \end{pmatrix}, \tag{30}$$

where $I_i(x,y)$ is the pixel value of the i-th image at (x,y). Next, this matrix is decomposed into three matrices (singular value decomposition):

$$\mathbf{A} = \begin{pmatrix} u_{1,1} & u_{1,2} & \dots & u_{1,N} \\ u_{2,1} & u_{2,2} & \dots & u_{2,N} \\ \vdots & \vdots & \ddots & \vdots \\ u_{N,1} & u_{N,2} & \dots & u_{N,N} \end{pmatrix} \begin{pmatrix} w_1 & & & 0 \\ & w_2 & & \\ & & \ddots & \\ 0 & & & w_N \end{pmatrix} \begin{pmatrix} V_1(1,1) & \dots & V_1(x,y) & \dots & V_1(x_n,y_m) \\ V_2(1,1) & \dots & V_2(x,y) & \dots & V_2(x_n,y_m) \\ \vdots & & \vdots & & \vdots \\ V_i(1,1) & \dots & V_i(x,y) & \dots & V_i(x_n,y_m) \\ \vdots & & \vdots & & \vdots \\ V_N(1,1) & \dots & V_N(x,y) & \dots & V_N(x_n,y_m) \end{pmatrix} \tag{31}$$

with $w_1 \sim w_2 \sim \ldots \sim w_N$. The decomposition is performed by functions in the C++ library[2]. Next, the coefficients of the linear combination of bases $V_i(x,y)$ are decided:

$$I_{\rm ref}(x,y) = c_1 V_1(x,y) + c_2 V_2(x,y) + \ldots + c_N V_N(x,y)\,, \tag{32}$$

where $I_{\rm ref}(x,y)$ are the pixel values of the reference image. The coefficients c_i are determined by minimizing

$$\sum_{x,y} \left(I_{\rm sci}(x,y) \quad I_{\rm ref}(x,y)\right)^2\,, \tag{33}$$

where $I_{\rm sci}(x,y)$ are the pixel values of the science image. As the $V_i(x,y)$ from an orthonormal system ($\sum_{x,y} V_i(x,y) \times V_j(x,y) = 0$), the coefficients are obtained as

$$c_i = \sum_{x,y} \frac{I_{\rm sci}(x,y) \times V_i(x,y)}{V_i(x,y)^2}\,. \tag{34}$$

Proceeding through the above steps, we built one reference image for each science image. The PSF residuals are smaller in PCA than in cADI.

[2]https://code.google.com/p/redsvd/wiki/Japanese

A.2 Difference between PCA and LOCI

Our PCA image processing is similar to LOCI processing (Lafrenière et al. 2007), but there are two differences between the methods.

One difference is the image separation technique. LOCI separates images into small arched pieces, and then builds reference images in each separation. The smaller separations bring the reference images closer to the science images. On the other hand, PCA does not set image separations. In cases of large residual noise in the halo (HD 15115 and HD 61005), we separate the annulus and build the reference images in each piece by PCA. However, we consider that the annulus separations limit the disk images to a lesser extent than arched separations for edge-on disks.

The other difference is the images used for building the reference images. Both methods construct the reference images from a linear combination of images, whereas LOCI constructs them from the science images themselves. PCA generates them from the orthonormal bases (principal components).